

# Accepted Manuscript

Diagenesis in salt dome roof strata: Barite - Calcite assemblage in Jebel Madar, Oman

Veerle Vandeginste, Manuela C. Stehle, Anne-Lise Jourdan, Harold J. Bradbury, Christina Manning, John W. Cosgrove



PII: S0264-8172(17)30215-5

DOI: [10.1016/j.marpetgeo.2017.06.008](https://doi.org/10.1016/j.marpetgeo.2017.06.008)

Reference: JMPG 2942

To appear in: *Marine and Petroleum Geology*

Received Date: 7 February 2017

Revised Date: 6 June 2017

Accepted Date: 6 June 2017

Please cite this article as: Vandeginste, V., Stehle, M.C., Jourdan, A.-L., Bradbury, H.J., Manning, C., Cosgrove, J.W., Diagenesis in salt dome roof strata: Barite - Calcite assemblage in Jebel Madar, Oman, *Marine and Petroleum Geology* (2017), doi: 10.1016/j.marpetgeo.2017.06.008.

This is a PDF file of an unedited manuscript that has been accepted for publication. As a service to our customers we are providing this early version of the manuscript. The manuscript will undergo copyediting, typesetting, and review of the resulting proof before it is published in its final form. Please note that during the production process errors may be discovered which could affect the content, and all legal disclaimers that apply to the journal pertain.

1 **Diagenesis in salt dome roof strata: barite - calcite assemblage in Jebel**  
2 **Madar, Oman**

3

4 Veerle Vandeginste<sup>1,2,\*</sup>, Manuela C. Stehle<sup>1</sup>, Anne-Lise Jourdan<sup>3</sup>, Harold J.  
5 Bradbury<sup>1</sup>, Christina Manning<sup>4</sup>, John W. Cosgrove<sup>1</sup>

6

7 <sup>1</sup>*Qatar Carbonate and Carbon Capture Research Centre and Department of Earth Science*  
8 *and Engineering, Imperial College London, Prince Consort Road, London, SW7 2BP, UK*

9 <sup>2</sup>*GeoEnergy Research Centre and School of Chemistry, University of Nottingham, University*  
10 *Park, NG9 2RD Nottingham, UK*

11 <sup>3</sup>*Bloomsbury Environmental Isotope Facility, UCL Earth Sciences, University College London,*  
12 *Gower Street, London, WC1E 6BT, UK*

13 <sup>4</sup>*Royal Holloway University of London, Dept. of Earth Science, Egham Hill, TW20 0EX, UK*

14 *\*Corresponding author: veerle.vandeginste@nottingham.ac.uk*

15

16

17 **Abstract**

18 Halokinesis causes a dynamic structural evolution with the development of faults and  
19 fractures, which can act as either preferential fluid pathways or barriers.  
20 Reconstructing reactive fluid flow in salt dome settings remains a challenge. This  
21 contribution presents for the first time a spatial distribution map of diagenetic phases  
22 in a salt dome in northern Oman. Our study establishes a clear link between  
23 structural evolution and fluid flow leading to the formation of diagenetic products  
24 (barite and calcite) in the salt dome roof strata. Extensive formation of diagenetic  
25 products occurs along NNE-SSW to NE-SW faults and fractures, which initiated  
26 during the Santonian (Late Cretaceous) and were reactivated in the Miocene, but not  
27 along the E-W fault, which was generated during Early Paleocene time. We propose  
28 that the diagenetic products formed by mixing of a warm (100°C) saline (17 wt%

29 NaCl eq.)  $^{87}\text{Sr}$  enriched ( $^{87}\text{Sr}/^{86}\text{Sr}$ : 0.71023) fluid with colder ( $35^\circ\text{C}$ ) meteoric fluid  
30 during Miocene to Pleistocene. The stable sulphur and strontium isotope composition  
31 and fluid inclusion data indicate that a saline fluid, with sulfate source derived from  
32 the Ara Group evaporite and Haima Supergroup layers, is the source for barite  
33 formation at about  $100^\circ\text{C}$ , predominantly at fault conjunctions and minor faults away  
34 from the main graben structure in the dome. In the Miocene, the saline fluid probably  
35 ascended along a halokinesis-related fault due to fluid overpressure (due to the rising  
36 salt and impermeable layers in the overlying stratigraphic sequence), and triggered  
37 the formation of barite due mixing with barium-rich fluids, accompanied by a drop in  
38 temperature. Subsequently, evolving salt doming with associated fault activity and  
39 erosion of the Jebel allows progressively more input of colder meteoric fluids, which  
40 mix with the saline warmer fluid, as derived from stable isotope data measured in the  
41 progressively younger barite-associated calcite, fault zone calcite and macro-  
42 columnar calcite. The reconstructed mixing model indicates a 50/50 to 90/10  
43 meteoric/saline fluid mixing ratio for the formation of fault zone calcite, and a 10 times  
44 higher concentration of carbon in the saline fluid end member compared to the  
45 meteoric fluid end member. The presented mixing model of salt-derived fluids with  
46 meteoric fluids is suggested to be a general model applicable to structural diagenetic  
47 evolution of salt domes world wide.

48

49 **Keywords:** diagenesis; halokinesis; salt; barite; isotopes; mixing

50

## 51 **1. Introduction**

52 Coupling reactive fluid flow with structural deformation in rocks overlying and  
53 surrounding salt bodies remains a challenge. We still need to improve our  
54 understanding of how dynamic deformation, fluid-rock interaction, and resulting  
55 changes in permeability and rock texture, are impacted by thermal and fluid salinity  
56 gradients linked to the presence of salt. Such knowledge is important for accurate

57 predictions in hydrocarbon exploration and safe long-term CO<sub>2</sub> storage. Rock salt  
58 has played an important role in hydrocarbon exploration, due to its sealing capacity  
59 and its potential for forming trapping structures such as folds and faults. Similarly,  
60 rock salt is currently considered as a seal for CO<sub>2</sub> storage reservoirs. Hence, this  
61 sedimentary rock type is important in applications that represent effective solutions to  
62 combat climate change, crucial to our society.

63 Besides its potential as sealing layer (Wang et al., 2015; Yang et al., 2015), rock salt  
64 is characterized by a low density and visco-elastic behavior compared to other  
65 sedimentary rock types, which makes salt prone to flow when denser layers overlie  
66 the lower density salt layers or due to tectonic stress. Salt flow generates  
67 deformation of the surrounding rocks, hence, the importance of salt tectonics in  
68 hydrocarbon exploration (Archer et al., 2012). Applying seismic acquisition to image  
69 salt diapirs is very challenging due to the strong acoustic impedance and velocity  
70 contrasts at the sediment – evaporite interface and complex shapes of steeply  
71 dipping flanks (Hudec and Jackson, 2007). Nevertheless, advances in structural  
72 models in salt tectonics have been achieved through sandbox experiments,  
73 theoretical models and field examples (Jackson and Vendeville, 1994; Vendeville,  
74 2005; Yin and Groshong, 2007; Yin et al., 2009), fluid flow models (Evans et al.,  
75 1991; Gradmann et al., 2012; Holzbecher et al., 2010; Ranganathan, 1992;  
76 Ranganathan and Hanor, 1989; Sarkar et al., 1995; Williams and Ranganathan,  
77 1994; Wilson and Ruppel, 2007), and 3-dimensional seismic datasets (Gamboa and  
78 Alves, 2016; Jackson and Lewis, 2016; Mattos et al., 2016; Omosanya and Alves,  
79 2013).

80 Salt domes studied at the surface provide excellent opportunities to collect field data  
81 that can be used subsequently as input feed or benchmarking for models. For  
82 example, a study that documents in detail the spatial distribution of fluid types and  
83 precipitation temperature of vein cements along La Popa salt weld in NE Mexico  
84 (Smith et al., 2012) is one of the few investigations published on the integration of

85 structures and reactive fluid flow in salt dome settings. A study on core samples from  
86 the Scotian Basin has also reported that active detachment faults on salt welds  
87 provide potential pathways and a source of salt for migrating formation water, leading  
88 to barite and sphalerite formation (Pe-Piper et al., 2015). A wide assemblage of  
89 diagenetic products can be found in salt dome cap rocks (Hallager et al., 1990).  
90 Barite is often a minor component among other minerals such as abundant metal  
91 sulphides, carbonates and elemental sulphur (Bechtel et al., 1996; Morrison and  
92 Parry, 1986; Sassen et al., 1994; Saunders and Thomas, 1996). Barite formation can  
93 be triggered as replacement of anhydrite by a decrease in temperature (Wagner et  
94 al., 2005), or by mixing of barium-rich fluids with sulphate-bearing fluids (Feng and  
95 Roberts, 2011; Greinert et al., 2002; Hanor, 2000; Tombros et al., 2015; Torres et al.,  
96 2003).

97 In the current paper, we report the study of structurally-controlled diagenesis in  
98 carbonate strata overlying a salt diapir in Jebel Madar (northern Oman). This salt  
99 dome in the Foothills of the central Oman Mountains is an excellent field site to  
100 investigate the evolution of paleofluid migration related to dynamic structural  
101 development during halokinesis, because of its great exposure, relatively easy  
102 access, extensive occurrence of diagenetic products (in particular barite and calcite),  
103 and the fact that it is not a surface-piercing salt dome (the salt does not occur in  
104 outcrop). The main objectives of this contribution are the following: (1) to document  
105 the spatial distribution of structurally-controlled diagenetic products in salt dome roof  
106 strata, (2) to determine the texture and geochemical signatures of the diagenetic  
107 products and paleofluids in salt dome roof strata, and (3) to link the paleofluid  
108 migration with structural evolution during halokinesis and reconstruct diagenetic  
109 product formation conditions. The integration of these datasets, with particular focus  
110 on the abundant presence of large barite crystals which have not been previously  
111 reported, combined with literature data, provides the reconstruction of diagenetic fluid  
112 migration in dynamic structural settings impacted by halokinesis.

113

114 **2. Geological setting**

115 Jebel Madar is a dome shaped, 500m-high mountain with an elliptical outline of 5 by  
116 8 km, and is situated in the Adam Foothills, south of the central Oman Mountains in  
117 Northern Oman (Fig. 1). The Jebel formed by diapirism of the Precambrian-Cambrian  
118 Ara salt (Mount et al., 1998) of the Ghaba Salt Basin. The Ghaba, Fahud and South  
119 Oman Salt Basins form the three evaporitic basins that are present in the deep  
120 subsurface of Interior Oman (Allen, 2007; Reuning et al., 2009). These basins are  
121 NE-SW oriented, and are interpreted to follow left-lateral, strike-slip faults in the  
122 basement (Loosveld et al., 1996). The Ara Salt was deposited coeval with the  
123 Hormuz Salt in Iraq, Iran, Kuwait and Pakistan (Allen, 2007; Edgell, 1991). The timing  
124 of diapirism is not well constrained, but it has been linked to separate events such as  
125 the initiation of ophiolite emplacement in the Late Cretaceous (Farzadi, 2006), or  
126 tilting of the eastern flanks of the salt basins during the Miocene Alpine  
127 compressional phase (Terken et al., 2001). Alternatively, a combination of events  
128 may have led to diapirism, with potentially minor salt movement having started in the  
129 Late Jurassic and followed by accelerated diapirism associated with the ophiolite  
130 obduction and the Alpine Orogeny (Ericsson et al., 1998; Peters et al., 2003). Still,  
131 the main doming event of Jebel Madar is probably linked with the Alpine Orogeny  
132 and thus of Miocene age (Claringbould et al., 2013).

133 The Late Neoproterozoic to Early Cambrian Ara Group consists of marine platform  
134 sediments representing at least six third-order cycles of carbonate to evaporite  
135 sedimentation (Schoenherr et al., 2010). These cycles are formed by Ara salt  
136 sedimentation at shallow depth followed by isolated platform carbonate deposits in  
137 deeper basins during transgression (Mattes and Morris, 1990). The Ara evaporite in  
138 the core of Jebel Madar dome consists mainly of halite, anhydrite which replaced  
139 primary gypsum (Mattes and Morris, 1990), and minor amounts of potash salts and  
140 Mg sulphates (Schroder et al., 2003).

141 The lithologies of the roof strata at Jebel Madar consist mainly of carbonate of  
142 Triassic to early Cretaceous age, belonging to the Hajar Supergroup (Fig. 2). This  
143 Supergroup consists of the Akhdar, Sahtan, Kahmah and Wasia Groups (Béchenec  
144 et al., 1993). The oldest formations, the Triassic Akhdar Group dolostone and  
145 Jurassic Sahtan Group sandstone and limestone crop out in the center of the Jebel,  
146 at a triple junction between the main faults (which created the Southwest Gully, East  
147 Gully and Sheep Valley), whereas the main part of the Jebel exposes Cretaceous  
148 Formations (Fig. 2). The Lower Cretaceous Kahmah Group consists of the Rayda,  
149 Salil, Habshan, Lekhwair, Kharaib and Shuaiba Formations. The three oldest  
150 formations in this Group form a prograding sequence of shallowing-upward facies  
151 with distal slope mudstone (shaly limestone and marls) of the Salil Formations, mid-  
152 ramp shoal ooidal and bioclastic grainstone and packstone of the Habshan  
153 Formation and inner platform algal mudstone, wackestone, bioclastic-peloidal  
154 grainstone and rudist-bearing packstone and floatstone of the Lekhwair Formation  
155 (Droste and van Steenwinkel, 2004). The latter is overlain by inner platform  
156 bioturbated, bioclastic (rudist-bearing) and peloidal packstone of the Kharaib  
157 Formation and (on top) the Shuaiba Formation. The Wasia Group comprises the  
158 Nahr Umr Formation, composed of shales and lime mudstones, and the Natih  
159 Formation with interfingering carbonate platform and intrashelf basin deposits of  
160 thickly-bedded mudstone, bioturbated wackestone, packstone and grainstone with  
161 abundant rudists and *Thalassinoides* burrows (Droste and van Steenwinkel, 2004).

162 The main formation of the Oman Mountains took place during the Alpine Orogeny  
163 Phase 2 (Eocene to Pliocene), whereas the area was earlier affected by the  
164 obduction of Semail ophiolite during Alpine Phase 1 (Turonian to Lower  
165 Maastrichtian) (Claringbould et al., 2013; Glennie, 2005; Gomez-Rivas et al., 2014;  
166 Mann and Hanna, 1990). The exact amount of burial underneath the Hawasina thrust  
167 sheets at the site of Jebel Madar is not accurately known, but was estimated at 1km  
168 by Claringbould et al. (2013) based on seismic sections from within a ten km range

169 from Jebel Madar. A detailed structural and stratigraphic map of Jebel Madar is  
170 presented by Claringbould et al. (2013). Other previous work on Jebel Madar  
171 documents dolomitization in the Habshan Formation (Vandeginste et al., 2013a) and  
172 Pleistocene phreatic calcite cave deposits (Immenhauser et al., 2007). The dominant  
173 calcite and barite diagenetic phases described in the current contribution occur  
174 mainly along previously mapped faults and fractures (Claringbould et al., 2013); only  
175 very small occurrences are more dispersed in the host rock or found in small patches  
176 or veins.

177

### 178 **3. Methodology**

179 For mapping the occurrence of barite and calcite cements along faults and fractures  
180 or in large vugs or caverns, we made use of Google Earth maps, the geological map  
181 of Claringbould et al. (2013), and a handheld Garmin Oregon GPS unit. GPS  
182 locations were recorded for our tracks, collected samples and structural  
183 measurements. A total of 249 hand samples were collected for this study, and a total  
184 of 154 structural measurements (including strike and dip of fractures and faults) using  
185 a Brunton compass.

186 Hand samples were cut, polished, etched with 1M HCl and stained with Alizarin Red  
187 S and potassium ferricyanide to distinguish calcite from other minerals (in particular  
188 dolomite and barite) following a procedure modified from Dickson (1966). Samples  
189 that were not identified as calcite by red or purple staining were subjected to X-ray  
190 diffraction analysis to determine the mineralogy, in particular to verify barite and  
191 detect potential presence of celestite (or lack thereof).

192 A total of 66 thin sections were examined using a Zeiss Axioskop 40 polarization  
193 microscope (with a connected Zeiss Axiocam ICc1 digital camera for  
194 photomicrographs) and a CITL cathodoluminescence (CL) Mk5-2stage mounted on a  
195 Nikon Eclipse 50i microscope (with an attached Nikon DS-Fi1c digital camera).  
196 Operating conditions for the CL stage were about 200  $\mu$ A and 13 kV.



197 For elemental analysis, sample powders of pure calcite and host rock were prepared  
198 by crushing small pieces of rock (cleaned with distilled water and dried overnight)  
199 using an agate mortar and pestle. An aliquot of 200 mg of each sample powder (144  
200 in total) was dissolved in 50 mL of a 5% HNO<sub>3</sub> solution (Vandeginste et al., 2013b).  
201 Analytical precision at the 95% confidence level determined on replicate analyses is  
202 about 15% for Ca, Mg, Al and Sr, and 10% for Fe and Mn.

203 Stable carbon and oxygen isotope analyses were carried out on more than 200  
204 carbonate samples. Aliquots of about 100 to 150 µg were reacted with phosphoric  
205 acid in a Thermo Scientific automated Kiel IV carbonate device at 70°C, and the  
206 resulting CO<sub>2</sub> gas was analysed in a MAT253 mass spectrometer. The carbon and  
207 oxygen isotopic values for carbonate samples are reported in per mil notation relative  
208 to Vienna Pee Dee belemnite (VPDB). Replicate analysis of NBS19 and Carrara  
209 Marble internal lab standards determined reproducibility better than 0.03‰ (1σ) for  
210 δ<sup>13</sup>C and 0.06‰ (1σ) for δ<sup>18</sup>O. Triplicates of samples show sample heterogeneity of  
211 0.13‰ (1σ) for δ<sup>13</sup>C and 0.12‰ (1σ) for δ<sup>18</sup>O.

212 Aliquots of 0.9 mg of barite were weighed and placed in silver capsules, and the  
213 oxygen isotopic composition was measured on a TC/EA pyrolysis-coupled IRMS  
214 Delta Plus XP ThermoFisher at CCiT at the University of Barcelona. Reproducibility of  
215 the oxygen isotope analysis is 0.2‰ (1σ, n = 2). Sulphur isotopes on barite samples  
216 were analysed by IsoAnalytical using EA-IRMS. The reference material used for  
217 analysis was IA-R061 (Iso-Analytical working standard barium sulphate, δ<sup>34</sup>S<sub>VCDT</sub> =  
218 +20.3‰). Repeated analysis of standard IA-R061 has a precision of 0.2‰ (1σ, n = 3)  
219 and repeated analysis of internal standard IAEA-SO-5 has a precision of 0.06‰ (1σ,  
220 n = 3).

221 For Sr isotope analyses, the pure calcite samples were dissolved in ~1mL dilute  
222 HNO<sub>3</sub>. Barite samples were leached in 6M HCl overnight, evaporated, and then  
223 dissolved in 2.5M HCl following the analytical procedure by Marchev et al. (2002).

224 Strontium was separated from the solutions using Eichrom Sr-spec resin, and  
225 analysed on a VG354 thermal ionization mass spectrometer at Royal Holloway  
226 University of London (UK). Samples were loaded on single Re filaments with a TaF  
227 emitter, and run using the multidynamic procedure of Thirlwall (1991). The SRM987  
228 standard ran with the samples gave a mean value of  $0.710256 \pm 0.000009$  ( $1\sigma$ ,  $N=9$ ).  
229 Fluid inclusions were studied in doubly polished wafers of calcite and barite cements  
230 on a Linkam THMSG600 heating-cooling stage. Since most (>90%) fluid inclusions  
231 observed were single-phase, the wafers were placed in a freezer overnight to  
232 generate two-phase fluid inclusions, a method described by Goldstein and Reynolds  
233 (1994), which was successful for barite, but not for calcite. Two-phase fluid inclusions  
234 appeared to stretch during rapid heating-cooling sequences in calcite, and hence, no  
235 reliable homogenization temperatures could be determined in calcite. Reproducibility  
236 of the final melting temperature of ice ( $T_m$ ) is within  $0.2^\circ\text{C}$  for both calcite and barite,  
237 and that of the homogenization temperature ( $T_h$ ) of barite samples is within  $2^\circ\text{C}$ .  
238 Inclusions in barite are susceptible to stretching and decrepitation during overheating  
239 (Ulrich and Bodnar, 1988). The barite minerals have not experienced higher  
240 temperature than the temperature they were formed at, given the indications for  
241 barite formation during halokinesis (and thus the uplift phase rather than burial).  
242 Overheating was avoided during microthermometric measurements by only heating  
243 each wafer piece till the homogenization temperature of the measured inclusions  
244 within that piece.

245

#### 246 **4. Macroscopic and petrographic characteristics of diagenetic products**

##### 247 *4.1. Barite*

248 Barite is found within host rock or co-occurs with barite-associated calcite within  
249 veins or large fractures. The host rock in which barite is found belongs to the  
250 Lekhwair (predominantly) and Kharaib formations. Typically, barite is present at the  
251 rim of the vein, whereas barite-associated calcite fills the inner space of the fractures

252 (Fig. 3A). Barite has generally tabular-shaped or lath-like euhedral crystals (of up to  
253 several centimeters wide), which are dispersed in the host rock (Fig. 3B) or more  
254 commonly form layers of radiating bundles (Fig. 3C). In some instances, barite is  
255 found as rosette structures of cross-cutting tabular crystals (Fig. 3D). Under crossed  
256 polarized light, barite is distinguished by its lower interference colours than that of  
257 calcite. Some fan-shaped barite crystals have sweeping extinction, but the lath-  
258 shaped crystals have homogeneous extinction. Bedding-parallel stylolites cross-cut  
259 the host rock and barite laths, but not the inclusion-poor barite-associated calcite.  
260 Calcite fills fractures within barite crystals (Fig. 4A-B). Barite is non-luminescent  
261 when viewed with the CL microscope.

262

#### 263 4.2. Calcite

264 Four types of calcite have been distinguished in this study based on their occurrence  
265 and characteristics, 1) thin calcite veins, 2) barite-associated calcite, 3) fault zone  
266 calcite, and 4) macro-columnar calcite. The first type of calcite occurs in thin (up to a  
267 few centimeters thick) veins within the host rock (Fig. 5A). These calcites have a  
268 crystal size < 1 cm and are blocky in shape.

269 The second type of calcite is present in meter-scale barite patches and in fractures  
270 that contain barite (Fig. 5B). Here, calcite fills space between the tabular barite  
271 crystals or they grow in the center of fractures on top of radiating barite crystals. In  
272 some diagenetic occurrences, calcite dominates over barite, and in those instances,  
273 barite forms small patches within larger calcite zones. Barite-associated calcite is  
274 crosscut by reddish brown silt (Fig. 6A) and macro-columnar calcite. The calcite  
275 crystals have homogeneous extinction and some contain two cross-cutting sets of  
276 faint, thick, cleavage twin planes, whereas other crystals have none or only fine, thin,  
277 cleavage twin planes. The latter crystals are in general light coloured and contain few  
278 inclusions. Under CL, calcite has a dull orange luminescence, commonly with lighter

279 and darker coloured zonations (Fig. 4B). Inclusion-free calcite is dull orange  
280 luminescent and cuts through barite.

281 The third type of calcite occurs as large calcite crystals of up to tens of centimeters  
282 long along major faults (Fig. 5C). These crystals are transparent and some have a  
283 faint white or greenish colour. In thin section, this calcite has relatively thick cleavage  
284 twinning planes (Fig. 4C) and a CL pattern of darker and lighter orange zonations  
285 (Fig. 4D).

286 The fourth type of calcite, macro-columnar calcite, is recognized in the field by its  
287 transparent crystals that can contain reddish colored zones (Fig. 5D) or co-occur with  
288 reddish brown silt layers (Fig. 6B). These crystals are generally a few, up to tens of  
289 centimeters long, and are commonly macro-columnar in shape, occasionally forming  
290 a radiating pattern (Fig. 5E). There are also white calcite rosettes which are topped  
291 by a reddish, thin layer (Fig. 5F). These rosettes grow upwards and are stacked upon  
292 each other, leaving some pore space in between them. The crystals in these  
293 structures are up to 5 cm long. The macro-columnar calcite has inclusion-poor calcite  
294 crystals (Fig. 4E) that display an inhomogeneous extinction pattern under crossed  
295 polarized light. The calcite is mainly non-luminescent under CL, but also displays  
296 some thin, dull orange luminescent zonations (Fig. 4F). Large veins filled with macro-  
297 columnar calcite crosscut fault zone calcite. Extensive calcite zones exhibit cross-  
298 cutting of multiple veins within larger vein zones, whereby the vein cement  
299 crosscutting all other vein cements is of the macro-columnar type with transparent  
300 and reddish crystal colour (Fig. 6C-E).

301

## 302 **5. Spatial distribution of barite and calcite types**

303 The distribution of barite and significant calcite type occurrences was mapped in  
304 Jebel Madar (Fig. 7). Most of the calcite mineralization is found near the three large  
305 structures (connected with each other in the center at the triple junction), whereas  
306 almost no mineralization apart from thin veins are found close to the rims of Jebel

307 Madar. The structural orientation of the fractures filled with different diagenetic  
308 products shows that the NNE-SSW to NE-SW trend is dominant and a second, NW-  
309 SE trend is of minor importance (Fig. 8). Both structural trends are represented in  
310 thin veins, but the larger structures with barite-associated calcite, fault zone calcite  
311 and macro-columnar calcite generally exhibit the dominant, NNE-SSW to NE-SW  
312 trend. Fractures filled with barite and barite-associated calcite are mainly NE-SW  
313 oriented, whereas the highest distribution of structures containing fault zone calcite  
314 and macro-columnar calcite is in NNE-SSW oriented fractures.

315 Barite is rare along the main, Southwest Gully NE-SW graben structure of the  
316 southwestern part of Jebel Madar, but is concentrated along other faults in the  
317 southern part of the Jebel (Hawk Valley) and three other occurrences slightly further  
318 away from the three main faults, especially where (minor) faults intersect (Fig. 7).  
319 There is a high concentration of macro-columnar calcite in an intensely fractured  
320 zone and cavern in the Shuaiba Formation in the southwestern corner of Jebel  
321 Madar (Sarg Valley), but some macro-columnar calcite also occurs along the main,  
322 Southwest Gully, NE-SW graben structure (mainly in the Shuaiba Formation), and is  
323 rare along faults in the northern (and northeastern) part of the Jebel (Sheep Valley  
324 and East Gully).

325

## 326 **6. Geochemical data of diagenetic products**

### 327 *6.1. Stable carbon, oxygen, sulphur and strontium isotope geochemistry*

328 The stable isotopic signature of limestone, barite and the different calcite types is  
329 presented in Supplementary File Table 1. The barite  $\delta^{18}\text{O}$  signature is between +19.8  
330 and +25.4‰ VSMOW; the  $\delta^{34}\text{S}$  of most barite samples falls between +27.0 and  
331 +37.6‰ VCDT, but two samples have a  $\delta^{34}\text{S}$  value of +47.9 and +48.8‰ VCDT (Fig.  
332 9, Supplementary File Table 1). For the stable isotope composition in the calcite  
333 types, both the average  $\delta^{13}\text{C}$  and  $\delta^{18}\text{O}$  (in ‰ VPDB) decrease in the following order:

334 from barite-associated calcite ( $\delta^{13}\text{C} = +2.8 \pm 0.5$  and  $\delta^{18}\text{O} = -4.5 \pm 1.2$ ), to thin calcite  
335 veins ( $\delta^{13}\text{C} = +2.5 \pm 1.2$  and  $\delta^{18}\text{O} = -4.8 \pm 1.8$ ), to fault zone calcite ( $\delta^{13}\text{C} = +0.5 \pm 1.0$   
336 and  $\delta^{18}\text{O} = -11.0 \pm 1.3$ ), and finally to macro-columnar calcite ( $\delta^{13}\text{C} = -5.5 \pm 1.4$  and  
337  $\delta^{18}\text{O} = -14.0 \pm 0.8$ ; Fig. 10, Supplementary File Table 1). From barite-associated  
338 calcite and thin calcite veins to fault calcite, the decrease in  $\delta^{18}\text{O}$  of about 6‰  
339 dominates (compared to 2‰ for  $\delta^{13}\text{C}$ ), whereas from fault calcite to macro-columnar  
340 calcite, the decrease in  $\delta^{13}\text{C}$  of about 6‰ (compared to 3‰ for  $\delta^{18}\text{O}$ ) is dominant  
341 (Fig. 10).

342 The average  $^{87}\text{Sr}/^{86}\text{Sr}$  ratios decrease from barite ( $0.71044 \pm 0.00055$ ), to barite-  
343 associated calcite ( $0.71000 \pm 0.00067$ ), to thin calcite veins ( $0.70991 \pm 0.00078$ ), to  
344 fault zone calcite ( $0.70935 \pm 0.00009$ ) and to macro-columnar calcite ( $0.70894 \pm$   
345  $0.00008$ ; Supplementary File Table 1; Fig. 11). This order is similar as observed for  
346 the trend in the stable oxygen and carbon isotope values. The spread in  $^{87}\text{Sr}/^{86}\text{Sr}$   
347 ratios between samples of the same phase is small for macro-columnar and fault  
348 zone calcite compared to the other calcite types. The limestone samples show a wide  
349 range in  $^{87}\text{Sr}/^{86}\text{Sr}$  data and the average value ( $0.70955 \pm 0.00038$ ) falls between that  
350 of fault zone calcite and that of thin calcite veins (Supplementary File Table 1).

351

## 352 *6.2. Major and minor element geochemistry*

353 The elemental content does not vary distinctly between different calcite types  
354 (Supplementary File Table 2). There is a weak positive correlation between Sr and  
355 Mg content, and the elemental composition of the different calcite types is similar for  
356 these two elements (Fig. 12A). The Ba content is highly variable among samples and  
357 the highest average values are obtained in the calcite cement and Kharaib Formation  
358 limestones, whereas the Shuaiba Formation limestones have the lowest average Ba  
359 content (Supplementary File Table 2). The main element that shows a clear trend  
360 between diagenetic phases is Mn, with a decreasing average content from barite-

361 associated calcite ( $187 \pm 66$  ppm), to thin calcite veins ( $151 \pm 75$  ppm) to fault zone  
362 calcite ( $128 \pm 26$  ppm) and to macro-columnar calcite ( $59 \pm 55$  ppm; Fig. 12B).

363

### 364 *6.3. Fluid inclusion study*

365 Barite as well as the calcite types studied contain mainly single-phase liquid  
366 inclusions of about 3 by 5 to 7 by 10  $\mu\text{m}$  large (Fig. 13). Homogenization temperature  
367 of generated two-phase primary fluid inclusions (after putting wafer in freezer) in  
368 barite ranges from 82 to 123°C (Supplementary File Table 3; Fig. 14A). Salinity in  
369 interpreted primary fluid inclusions, derived from final ice melting temperatures using  
370 the equation of Goldstein and Reynolds (1994) is around 21 wt% NaCl eq in barite,  
371 and decreases in the different calcite types, from 17 wt% NaCl eq in barite-  
372 associated calcite, to 2 to 4 wt% NaCl eq in two samples of fault-zone calcite, to 0.1  
373 wt% NaCl eq in macro-columnar calcite (Fig. 14B). The salinity in the calcite types  
374 shows a positive correlation with the  $\delta^{18}\text{O}$  values of the calcite samples measured,  
375 i.e. higher salinity corresponds to higher  $\delta^{18}\text{O}_{\text{calcite}}$  values (Fig. 14B). First hydrous salt  
376 melting temperatures in barite between -53 and -45°C indicate a saline aqueous  
377 system with predominantly  $\text{CaCl}_2$ , whereas the first hydrous salt melting temperature  
378 in fluid inclusions in barite-associated calcite between -34 and -23°C (Supplementary  
379 File Table 3) indicate a saline system dominated by NaCl with minor addition of KCl  
380 and  $\text{CaCl}_2$ .

381

## 382 **7. Discussion**

### 383 *7.1. Diagenetic barite-calcite assemblage in salt dome roof strata*

384 Diagenetic products in strata overlying a salt diapir are likely to be influenced by the  
385 presence of the salt as well as by the structural deformation related to the halokinesis  
386 (Archer et al., 2012). Previous diagenetic work on five sampling sites in Jebel Madar  
387 concentrated mainly on phreatic cave deposits with macro-columnar calcite,

388 identified traces of barite, and included some fault zone calcite (Immenhauser et al.,  
389 2007). The novelty in our study involves the exploration of the entire Jebel to  
390 document the spatial distribution of all diagenetic phases present in the strata  
391 overlying the salt diapir, as observed in outcrop, with an important focus on  
392 significant barite occurrences, and the link to structures (Fig. 7).

393 We distinguished different diagenetic cements, i.e. barite and several calcite types,  
394 based on their mineralogy and textural and geochemical characteristics. The  
395 abundance of large barite crystals in Jebel Madar has not been previously reported.  
396 In contrast to calcite, which is a common diagenetic product in sedimentary strata,  
397 barite (barium sulphate) is more rare, but not uncommon in salt dome settings  
398 (Warren, 2000). Salt diapirs are often overlain by a caprock consisting of an  
399 anhydrite zone and overlying carbonate zone with anhydrite, gypsum, elemental  
400 sulphur, metal sulphides such as pyrite, sphalerite and galena, and Sr and Ba  
401 minerals such as barite, celestite and strontianite (Sassen et al., 1994; Saunders and  
402 Thomas, 1996; Souissi et al., 2007).

403 Barite occurring in the roof strata of the Jebel Madar salt dome has large (up to  
404 centimeter scale) crystals, which have a rhombohedral, tabular shape, present as  
405 single lath-shaped crystals, as radiating bundles organized in layers separated by  
406 thin dark coatings, or as rosettes. The rhombohedral morphology suggests that the  
407 barite formed via surface reaction growth mechanisms from a solution with a low  
408 degree of barite saturation, in contrast to highly saturated fluids which favour the  
409 precipitation of dendritic (rod-like, spindle-like, star-like) barite crystals by diffusional  
410 transport (Dunn et al., 1999; Shikazono, 1994). The barite rosettes indicate growth in  
411 open space, as they are still present in cavities, which is consistent with growth in  
412 extensional fault zones (Balsamo et al., 2016).

413 The large size of the barite crystals contrasts strongly with the micrometer scale of  
414 marine pelagic barite (Bertram and Cowen, 1997; Dehairs et al., 1980; Griffith and  
415 Paytan, 2012), and indicates formation at elevated temperature, as confirmed by fluid



416 inclusion microthermometric data ( $> 80^{\circ}\text{C}$ ). We must note, though, that the fluid  
417 inclusion homogenization temperature data in barite need to be treated with caution.  
418 Barite has good cleavage and a low bulk modulus and often contains single-phase  
419 fluid inclusions alongside two-phase inclusions, even for formation conditions at  
420  $150^{\circ}\text{C}$ , and this may be caused by overpressuring of fluids in the inclusions linked to  
421 post-entrapment deformation of barite (Badhe and Pandalai, 2015). Nevertheless, in  
422 addition to the barite crystal morphology and size and the formation temperature of  
423 about  $110^{\circ}\text{C}$  of barite-associated calcite (see below), it can be concluded that barite  
424 formed at elevated temperature.

425 Crosscutting relationships indicate that barite is older than the documented calcite  
426 types, and that macro-columnar calcite is younger than fault zone calcite, itself  
427 postdating barite-associated calcite (Fig. 3, 5-6, 15). The type and diversity of  
428 diagenetic products forming in the neighbourhood of salt diapirs relate to the  
429 diagenetic process involved, determined by the setting, such as migrating fluids, host  
430 rock, and temperature. The presence of barite and the lack of sulphides suggest  
431 predominance of sulphate over sulphide implying the lack of or very limited sulphate  
432 reduction, a process common in settings containing organic-rich sediments with  
433 sulphate-reducing bacteria or hydrocarbons (Cai et al., 2005; Machel, 2001;  
434 Vandeginste et al., 2006; Vandeginste et al., 2009).

435

### 436 *7.2. Paleofluid flow pathways and evolution through time*

437 The abundant large diagenetic products present within the faults and fractures in the  
438 dome testify to the important role of these structures as preferential fluid pathways.  
439 Fault zones have also been documented to be major fluid pathways in other jebels in  
440 the Adam Foothills in northern Oman (Mozafari et al., 2015). The stress field that  
441 controlled and generated the faults and fractures in the carbonate strata overlying the  
442 salt diapir in Jebel Madar is thought to be controlled both by the local stress field  
443 linked to salt diapirism itself, as well as to regional tectonics (Claringbould et al.,

444 2013; Quinta et al., 2012). The paragenesis of the cement types (Fig. 15) can thus  
445 reveal information on the evolution of structures during halokinesis and the interplay  
446 between regional tectonics and local stress caused by salt doming.

447 The orientation of thin calcite veins is variable, but the dominant orientation of barite-  
448 associated calcite structures (NE-SW) is similar to that of structures filled with fault  
449 zone calcite and macro-columnar calcite (NNE-SSW). Hence, the NE-SW to NNE-  
450 SSW structures were the main pathways for fluids from which the diagenetic  
451 products formed. In contrast, no significant occurrence of diagenetic products was  
452 observed along the E-W fault, suggesting lack of fluid migration along E-W  
453 structures. The orientation of the main structures and also the shape of Jebel Madar  
454 indicate that the NE-SW trend dominated the elongated dome shape and the normal  
455 faulting during halokinesis. This NE-SW trend is interpreted to relate to pre-existing  
456 normal faults of Precambrian age present in the basement, which probably also  
457 controlled the location of the diapir (Claringbould et al., 2013; Immenhauser et al.,  
458 2007).

459 Despite the challenges in the interpretation of the major structures in Jebel Madar,  
460 Claringbould et al. (2013) suggests that the development of the structures occurred  
461 in three phases: 1) Late Cretaceous dome initiation and the formation of NE-SW  
462 fractures followed by the development of grabens and cementation, 2) Early  
463 Paleocene E-W dextral strike-slip faulting with lack of cementation, and 3) Miocene  
464 reactivation and inversion of faults and a final period of diapirism and dome.  
465 However, petrographic and geochemical (notably radiogenic dating) data from  
466 macro-columnar calcite suggests that these cements were deposited during the  
467 Pleistocene to Holocene (Immenhauser et al., 2007). Based on these previous  
468 studies and the data presented in the current contribution, we propose that the  
469 structural evolution follows that proposed by Claringbould et al. (2013), but that major  
470 barite and calcite cementation only started in the Miocene and not in the Late  
471 Cretaceous. Claringbould et al. (2013) interpreted down-dip slickenlines on calcite

472 fault surfaces as an argument to suggest abundant burial calcite cementation along  
473 NE-SW fault zones in Late Cretaceous time, and then reactivation of those faults in  
474 the Miocene. In contrast, we hypothesise that the NE-SW faults and fractures  
475 developed during Late Cretaceous time, but that abundant cementation occurred  
476 during reactivation and final dome formation during Miocene to Pleistocene times,  
477 during which several pulses and episodes of fluid flow and NE-SW fault reactivation  
478 occurred (Fig. 16).

479 Seismic sections and interpretations by Claringbould et al. (2013) show that salt  
480 doming has caused an uplift of about 2 to 2.5 km (in the centre of the dome).  
481 Reported salt diapirism induced uplift rates are in the order of 2 to 8 mm per year in  
482 the center of a dome (Bruthans et al., 2006; Pe'eri et al., 2004). These uplift rates  
483 suggest that salt diapirism in Jebel Madar causing 2 km uplift could have happened  
484 in about 250 to 1000 kyr. Since there are no outcrops of post-Natih Formation age, it  
485 can be argued that at least 1.5 km of material has been eroded either during or  
486 immediately after salt doming. High end values of denudation rates of about 0.1 mm  
487 per year (Kirchner et al. 2001) support erosion of a 1.5 km thick package in a time  
488 period of about 15 Myr. These calculations indicate that it is plausible that the  
489 diagenetic products resulted from fluid flow pulses along the major faults during  
490 dome formation in the last 15 million years. This model is supported by the Miocene  
491 to Pleistocene age of the cements, formed by mixing of fluids, as discussed below.

492 The spatial distribution of the diagenetic products elucidates further the sequence of  
493 cement precipitation along structures in the Jebel, and thus helps to reconstruct fluid  
494 migration during halokinesis. Fault zone calcite is present along each major fault,  
495 except for the NE-SW fault near Hawk Valley in the southern part of the Jebel, which  
496 is cemented by barite and barite-associated calcite (Fig. 7). Since the latter are the  
497 oldest diagenetic products in the paragenesis (Fig. 15), we interpret that fluid  
498 migration focused first along this Hawk Valley NE-SW fault. Only minor amounts of  
499 barite have been documented along the main, Southwest Gully, NE-SW graben

500 structure, where more focused fluid migration took place subsequently during  
501 abundant formation of fault zone calcite. Macro-columnar calcite is present along NE-  
502 SW faults (postdating fault zone calcite) and is especially abundant in the  
503 southwestern zone (and previously documented eastern area) in Shuaiba Formation  
504 host rock. Moreover, macro-columnar calcite has been documented in the Shuaiba  
505 Formation away from the main faults in the eastern part of Jebel Madar  
506 (Immenhauser et al., 2007). Hence, besides the structural control, there is also a  
507 sedimentologic control at least on the spatial distribution of the macro-columnar  
508 calcite. The abundance in the Shuaiba Formation relates to its stratigraphic position  
509 underneath the Nahr Umr seal, as formation fluids were trapped and dissolution  
510 affected the host rocks, causing solution-enhanced fractures and caverns due to  
511 cooling of formation waters during halokinesis-induced uplift before cementation  
512 (Immenhauser et al., 2007).

513 In conclusion, cementation occurs first from fluids (generating barite and barite-  
514 associated calcite) focused along minor faults and conjunctions at sites several  
515 kilometers apart spread within the Jebel, subsequently from fluids along NE-SW  
516 faults with abundant fault-zone calcite precipitation along the major NE-SW fault, and  
517 finally from fluids focused mainly in the southwestern and eastern zone along NNE-  
518 SSW to NE-SW structures and in the Shuaiba Formation, generating macro-  
519 columnar calcite.

520

### 521 *7.3. Origin and formation process of barite*

522 Dissolution of evaporites is one of the main origins of subsurface brines in  
523 sedimentary basins, besides subaerial evaporation of seawater and membrane  
524 filtration (Hanor, 1994). The evaporites, such as anhydrite or other sulphate minerals,  
525 at the core of a salt dome, are a likely source of sulphate for barite formation in this  
526 setting, similar to examples in other studies where sulphates and sulphides formed in  
527 evaporite settings (Warren, 2000). Jebel Madar formed in response to diapirism of

528 the Late Neoproterozoic to Early Cambrian Ara Group evaporite, consisting mainly of  
529 halite, anhydrite which replaced primary gypsum (Mattes and Morris, 1990), and  
530 minor amounts of potash salts and Mg sulphates (Schroder et al., 2003).

531 Fluid inclusion measurements indicate that barite and barite-associated calcite  
532 precipitated from highly saline fluids (21 and 17 wt% NaCl eq, respectively) probably  
533 at around 100°C. Fluid inclusion measurements in barite need to be treated with  
534 caution, as mentioned above. Although the fact that the fluid inclusion assemblage is  
535 dominated by single-phase inclusions generally suggests a mineral formation  
536 temperature of less than 40 to 60°C, it is not uncommon for small inclusions (< 3 µm)  
537 to be single-phase aqueous inclusions even though the homogenization temperature  
538 is as high as 100°C (Goldstein and Reynolds, 1994). Clumped isotope data  
539 corroborate formation at burial conditions with a barite-associated calcite formation  
540 temperature of around 110°C (John et al., 2014). Moreover, dissolution of anhydrite  
541 has been documented at about 110°C based on reflectance data from pore-filling  
542 solid bitumen in caprock of the exposed salt domes in the Ghaba Salt Basin  
543 (Reuning et al., 2009).

544 Further supporting evidence for the elevated temperature formation of barite and  
545 barite-associated calcite is provided by the oxygen isotope geothermometer,  
546 assuming that the co-occurring calcite and barite formed under very similar  
547 conditions (similar fluid and temperature) and under equilibrium oxygen isotope  
548 fractionation. Taking the average oxygen isotope composition of barite (+22.8‰  
549 VSMOW) and barite associated calcite (+26.3‰ VSMOW), we calculate a formation  
550 temperature of 90°C and 115°C, based on the oxygen isotope fractionation of barite  
551 – saline water (Kusakabe and Robinson, 1977) and of calcite – water from Friedman  
552 and O'Neil (1977) and Demeny et al. (2010), respectively:

$$1000 \ln \alpha_{cc-bar} = 0.14 \frac{10^6}{T^2} + 2.41$$

553

$$1000 \ln \alpha_{cc-bar} = -2.64 \frac{10^5}{T^2} + 17.599 \frac{10^3}{T} - 24.34$$

554

555 The sulphate source for barite formation is confirmed by sulphur isotope data. The  
556  $\delta^{34}\text{S}$  in barite in Jebel Madar ( $+31 \pm 3$  ‰ VCDT) is typical for the sulphate  
557 composition of Late Neoproterozoic to Early Cambrian seawater (Claypool et al.,  
558 1980), suggesting that the source of sulphate was Ara Group evaporite. Seawater  
559 and associated sulphate deposits of younger age are characterized by a much lower  
560  $\delta^{34}\text{S}$  value (Claypool et al., 1980; Paytan et al., 2004; Rees et al., 1978). There is a  
561 good match between the measured  $\delta^{34}\text{S}$  values in barite of Jebel Madar and that in  
562 Late Neoproterozoic to Early Cambrian anhydrite from Siberia and India (Banerjee et  
563 al., 1998; Claypool et al., 1980; Strauss et al., 2001). Moreover, the barite data in this  
564 study overlap both with the sulphur isotope values from anhydrite cements in the  
565 Haima Supergroup in the Fahud Salt Basin, i.e.  $+20.4$  to  $+30.6$ ‰ VCDT (Ramseyer  
566 et al., 2004) and those of the Ara Group anhydrite in the South Oman Salt Basin, i.e.  
567  $+32.4$  to  $+46.4$ ‰ VCDT (Schroder et al., 2004) and plot predominantly between the  
568 averages of those datasets (Fig. 9). Schroder et al. (2004) invoked the process of  
569 bacterial sulphate reduction to explain the elevated  $\delta^{34}\text{S}$  signature in anhydrite in the  
570 South Oman Salt Basin compared to the sulphate composition in Late  
571 Neoproterozoic to Early Cambrian deposits from other parts of the world, based on  
572 the presence of organic-rich source rocks underlying and interbedded with the Ara  
573 Group evaporites (Mattes and Morris, 1990; Schoenherr et al., 2009), and source  
574 rocks present in the Ghaba Salt Basin (Reuning et al., 2009). The sulphate origin of  
575 barite in Jebel Madar thus represents a mixing of two sources: dissolved sulphate  
576 from the Ara Group and from the Haima Supergroup.

577 The extensive occurrence of barite along faults in the salt dome, when considered in  
578 concert with the identified source for sulphate, suggests that sulphate-rich fluids  
579 preferentially migrated along halokinesis-related faults and fault conjunctions. The  
580 driving force for the ascent of the fluids is not entirely certain. The pressure exerted

581 by the rising salt upon the overlying stratigraphic sequence, which includes  
582 impermeable layers such as shale units in the Haima Supergroup, the Haushi Group  
583 and the Nahr Umr Formation, can have led to fluid overpressure, and the release of  
584 those overpressured fluids during fault activity. Another potential scenario considers  
585 upward release of fluids linked to the decrease in overburden pressure due to uplift  
586 during salt doming and erosion at the surface. Such scenario is derived from the  
587 decompression model of extension-driven dewatering due to the strong difference in  
588 compressibility between rocks and fluids leading to overpressuring of pore fluids  
589 during denudation (Staude et al., 2009). In both scenarios, the ascent of the fluids  
590 would have been accompanied by a drop in temperature and pressure, which might  
591 have been a trigger for the precipitation of barite (Fig. 16). A drop of 200°C to 100°C  
592 (given a pressure of 500 bar) would result in the precipitation of up to 84 mg of barite  
593 per kg of fluid (Blount, 1977) assuming a 3M NaCl fluid based on our fluid inclusion  
594 data. Nevertheless, barite precipitation in burial settings has generally been attributed  
595 to mixing of fluids, because sulphate and barium (chloride) tend to not be transported  
596 together in fluids. Therefore, the ultimate trigger for barite precipitation may have  
597 been mixing of the ascending sulphate-rich brine (migrating along the fault) with a  
598 barium-rich fluid (most likely from formation fluids derived from interaction with  
599 barium-rich shales). Such conceptual model considers relatively fast advective fluid  
600 flow of sulphate-rich brines through fractures in the fault zone, which is typically  
601 episodic and cyclic linked with fault activity (Sibson, 1992) and involves elevated fluid  
602 pressure (Bons et al., 2012). This fault zone fluid flow alternates with episodes of  
603 relatively slow pervasive advective flow of barium-rich fluids through permeable  
604 formations (driven by convection in the aftermath of warm fluid migration along the  
605 fault) and important diffusional mass transport when fluid pressure is low (Wagner et  
606 al., 2010). Fluid mixing during fault activity in this case is most likely achieved by  
607 hydrodynamic dispersion (Bons et al., 2012).

608

609 *7.4. Origin and formation process of calcite phases*

610 Calcite precipitation can be triggered by several factors and is a common diagenetic  
611 product. In salt dome settings, it has been reported to form at about 70 to 100°C from  
612 saline (5 to 20 wt% NaCl eq.) fluids (Morrison and Parry, 1986). It has also been  
613 postulated that CO<sub>2</sub> generated through degradation of organic matter (e.g.,  
614 petroleum, methane) is an important source for calcite cement in carbonate cap rock  
615 (Bechtel et al., 1996). However, the latter mechanism is unlikely to explain the origin  
616 of calcite in Jebel Madar, since  $\delta^{13}\text{C}$  is higher than -8‰ VPDB (Supplementary File  
617 Table 1), and the involvement of degradation of organic matter would lead to lower  
618  $\delta^{13}\text{C}$  values (Machel, 2001).

619 Similar to the stable isotope data of calcite in our study, Immenhauser et al. (2007)  
620 showed a decrease in  $\delta^{18}\text{O}$  and especially  $\delta^{13}\text{C}$  from fault zone calcite to macro-  
621 columnar calcite from Jebel Madar. Those authors interpreted that phreatic cave  
622 calcite in Jebel Madar formed by mixing of a saline hydrothermal fluid and a meteoric  
623 fresh water fluid (with incorporation of soil-derived light carbon). Also, Reuning et al.  
624 (2009) documented similar co-varying  $\delta^{13}\text{C}$  and  $\delta^{18}\text{O}$  trends from carbonate stringers  
625 of the surface-piercing salt domes from the Ghaba Salt Basin, and mixing of fluids  
626 with an additional source for lower  $\delta^{13}\text{C}$  values linked to oxidized organic matter from  
627 liquid hydrocarbons consumed during sulphate reduction (Reuning et al., 2009). In  
628 addition to these previous studies in the area, we have documented the full  
629 assemblage of diagenetic components in the system found at the surface of the  
630 Jebel Madar dome and this is presented within a geospatial and structural  
631 framework.

632 The  $^{87}\text{Sr}/^{86}\text{Sr}$  data also display distinct signatures for different diagenetic phases. The  
633  $^{87}\text{Sr}/^{86}\text{Sr}$  composition of fault zone calcite (0.7094) is close to that of Ara Group  
634 carbonate (0.7092) in Oman (Burns et al., 1994), whereas macro-columnar calcite  
635 has  $^{87}\text{Sr}/^{86}\text{Sr}$  values of  $\leq 0.7090$ , and the  $^{87}\text{Sr}/^{86}\text{Sr}$  values of barite-associated calcite



636 and thin calcite vein samples range from 0.7092 up to 0.7110, indicating  $^{87}\text{Sr}$   
637 enrichment. The latter enrichment is interpreted to originate from incorporation of  $^{87}\text{Sr}$   
638 through liberation of Rb by aluminosilicate reactions (clay mineral reactions or K-  
639 feldspar dissolution) in the Haima Supergroup (Ramseyer et al., 2004), and this is  
640 consistent with the interpretation that the barite-forming fluids interacted with the  
641 Haima sandstones and the Ara anhydrite, as also derived from the sulphur isotope  
642 data.

643 The stable isotope and fluid inclusion data from both this work and previous work  
644 support formation of the diagenetic assemblage by mixing of fluids. We propose  
645 hereby that the high temperature saline end member is around 100°C, as derived  
646 from the barite formation temperature (and supported by clumped isotope barite-  
647 associated calcite formation temperature), and that the low temperature meteoric end  
648 member is around 35°C. We can then link the stable oxygen isotope data and the  
649 strontium isotope data to these end members and model mixing of those end  
650 members at different ratios (Appendix 1). For this model, we derive the  $\delta^{18}\text{O}_{\text{fluid}}$  of  
651 +10.9‰ VSMOW based on  $\delta^{18}\text{O}_{\text{calcite}}$  of -2.5‰ VPDB from barite-associated calcite  
652 formed at 100°C, and  $\delta^{18}\text{O}_{\text{fluid}}$  of -10.4‰ VSMOW based on  $\delta^{18}\text{O}_{\text{calcite}}$  of -14.4‰  
653 VPDB from macro-columnar calcite formed at 35°C using the equation of Friedman  
654 and O'Neil (1977). This low temperature end member  $\delta^{18}\text{O}_{\text{fluid}}$  signature is consistent  
655 with meteoric water from Southern Oman (Fleitmann et al., 2003). The stable oxygen  
656 isotopic signature of the macro-columnar calcite and reconstructed  $\delta^{18}\text{O}_{\text{fluid}}$  are  
657 consistent with interpretations presented by Immenhauser et al. (2007) based on a fit  
658 between fluid inclusion  $\delta\text{D}$  values, the Southern Oman meteoric water line,  $\delta^{18}\text{O}_{\text{calcite}}$ ,  
659 and derived temperature. The calculated high-temperature end member  $\delta^{18}\text{O}_{\text{fluid}}$   
660 value is consistent with basinal fluids that have dissolved Ara Group anhydrite based  
661 on the fact that  $\delta^{18}\text{O}_{\text{sulphate}}$  in Neoproterozoic to Early Cambrian seawater is about

662 +14‰ VSMOW (Bottrell and Newton, 2006; Claypool et al., 1980; Longinelli and  
663 Craig, 1967).

664 The model of fluid mixing is presented using the end member data for temperature,  
665  $\delta^{18}\text{O}_{\text{fluid}}$ , fluid inclusion salinity, and  $^{87}\text{Sr}/^{86}\text{Sr}$  data (Fig. 17). Based on the mixing  
666 temperature and  $\delta^{18}\text{O}_{\text{fluid}}$  values, the  $\delta^{18}\text{O}_{\text{calcite}}$  values for different mixing ratios were  
667 reconstructed for this model (Fig. 17B). For temperature,  $\delta^{18}\text{O}_{\text{fluid}}$ , fluid inclusion  
668 salinity, and  $^{87}\text{Sr}/^{86}\text{Sr}$  signatures, simple mixing using different fractions for the saline  
669 end member and the meteoric end member was applied (Appendix 1). For the  $\delta^{13}\text{C}$   
670 signature, the data show that no simple mixing of the two end member fluids is  
671 applicable. Here, the data indicate that carbon concentrations in the end member  
672 fluids were different, and a model taking account of 10 times higher concentration of  
673 carbon in the saline end member compared to the meteoric end member provides a  
674 good match for the observed data (Fig. 17B; Appendix 1). Our model assumes here  
675 that the signatures measured attribute to the signature of the fluids involved in the  
676 mixing model, and no local diffusion effects on the very small scale have been  
677 corrected for. Given the large scale of the diagenetic products, i.e. cm-sized crystals  
678 and meters to tens of meters wide fault zones, assuming predominantly fluid  
679 advective processes for mass transfer is justified for the interpretation of the calcite  
680 formation conditions and the relatively short time scale. However, diffusive processes  
681 played a role in the formation of thin calcite veins, and in the processes involved in  
682 the origin of the end member fluids (such as  $^{87}\text{Sr}$  enrichment in sulphate-bearing  
683 fluids due to fluid-rock interaction).

684 In terms of the hydrodynamic feasibility of the mixing model, we would like to  
685 emphasize that our model does not involve simultaneously ascending and  
686 descending fluid migration along fault zones but is a dynamic model with two end  
687 member fluids. In Miocene time, episodes of ascending fluid migration occurred  
688 during fault activity and led to the formation of barite and subsequently barite-

689 associated calcite. These episodic events brought batches of saline fluid higher up  
690 along the fault zone, similar to the model of mobile hydrofractures suggested by Bons  
691 (2001). Meteoric fluids at the exposed surface caused weathering and erosion during  
692 uplift related to salt doming. With time, the exposed sedimentary package overlying  
693 the salt diapir became thinner, and hence meteoric fluids reached stratigraphically  
694 older formations. Saline fluids ascended during fault activity, whereas migration of  
695 meteoric fluids was probably more important during interseismic periods with low fluid  
696 pressure. The removal of the impermeable Nahr Umr Formation in the centre of the  
697 salt dome probably implied that no more ascending overpressured fluids were  
698 released along the faults. Instead, topographically-driven meteoric fluid flow became  
699 predominant along the exposed faults and in stratigraphic layers underlying the Nahr  
700 Umr Formation. These meteoric fluids mixed with the saline fluids that had ascended  
701 along the fault zones earlier.

702 The diversity of diagenetic products found in strata overlying salt domes is thus  
703 highly impacted by the origin of the end member fluids which likely involved  
704 interaction with anhydrite in the salt dome and overlying/surrounding carbonate and  
705 siliciclastic strata, and be influenced by other factors, such as the presence of  
706 organic rich strata or hydrocarbons. Mixing of fluids is a key mechanism triggering  
707 precipitation of minerals in salt dome settings. The barite-associated calcite formed  
708 by a predominant contribution of the saline end member fluid, whereas macro-  
709 columnar calcite formed by a dominant contribution of the meteoric fluid end  
710 member. Our model shows that the fault-zone calcite formed from around 50/50 to  
711 90/10 ratio of meteoric/saline end member fluids (Fig. 17). The geochemical nature of  
712 the diagenetic products and their paragenesis reflect the structural evolution of the  
713 salt dome and related fluid flow with initially saline brines from interaction with the  
714 salt, and then a progressively larger contribution from meteoric fluids, probably linked  
715 with salt doming related uplift and infiltration of meteoric fluids along fault zones.

716

717 **8. Conclusions**

718 This study identified major barite and calcite diagenetic products in salt dome roof  
719 strata. Barite, barite-associated calcite, fault zone calcite and macro-columnar calcite  
720 occur all predominantly along NE-SW to NNE-SSW structures, which are interpreted  
721 to be templated by regional Precambrian basement faults, and no major diagenetic  
722 cementation is found along E-W faults. The spatial distribution of diagenetic products  
723 is not homogeneous among faults, and barite is concentrated in fault conjunctions  
724 and in the Hawk Valley fault zone parallel to, but away from, the main NE-SW graben  
725 structure of the Southwest Gully. The barite rosettes of cross-cutting, tabular, large  
726 crystals formed at about 100°C in cavities linked to extensional fracturing during  
727 halokinesis. Barite sulphur isotope data indicate a mixed source with dissolved  
728 sulphate from the Ara Group and from the Haima Supergroup, the latter also  
729 contributing enriched  $^{87}\text{Sr}$  to the diagenetic fluids. Salt doming resulted in fracturing  
730 of roof strata, creating pathways for fluid migration. Barite precipitation was probably  
731 triggered by mixing of an ascending sulphate-rich fluid and a barium-rich fluid. The  
732 transition of barite to barite-associated calcite precipitation could be controlled by a  
733 limitation in the barium supply. Mixing of the saline fluids with colder meteoric fluids  
734 has caused precipitation of fault zone calcite and macro-columnar calcite. The  
735 paragenetic sequence of the diagenetic products indicating an increase in the  
736 meteoric fluid component reflects the ongoing salt doming with uplift and extensional  
737 fault zone activity, and thus more extensive charging of meteoric fluids compared to  
738 the higher temperature saline fluids. Formation of the diagenetic products probably  
739 occurred over Miocene to Holocene time. The geochemical signatures measured in  
740 the diagenetic products fit a mixing model of a warm saline fluid and a colder  
741 meteoric fluid. Similar tectonic, hydrologic and fluid mixing evolution as derived for  
742 Jebel Madar can be expected in salt dome roof strata in other regions worldwide.  
743 Moreover, the methods (including structural diagenetic mapping) and modelling

744 techniques presented here can be applied in a range of other case studies that  
745 involve fluid migration along structures.

746

#### 747 **Acknowledgements**

748 This research was funded by Qatar Petroleum, Shell and the Qatar Science and  
749 Technology Park (QSTP) and by the Stephen E. Laubach Research in Structural  
750 Diagenesis Award, granted by the Sedimentary Geology and the Structural Geology  
751 and Tectonics Divisions of the Geological Society of America. Field logistics were  
752 handled by Shuram. We acknowledge some field and lab work done by Janine Lahr  
753 at an early stage of this project. We would like to thank Emma Williams and Stanislav  
754 Strekopytov (ICP-AES) and Simon Davis (stable isotopes) for their help with various  
755 analytical techniques. Sulphur isotopes in barite were measured by IsoAnalytical. We  
756 thank Rosa Marimon from CCiT of the University of Barcelona for providing the  
757 oxygen isotope analyses in barite. We also thank Conxita Taberner for scientific  
758 discussions. We are very grateful to the associate editor Enrique Gomez-Rivas and  
759 the reviewers Mark Fischer and an anonymous reviewer for their valuable comments  
760 and suggestions which helped to improve the content and presentation of this  
761 manuscript.

762

#### 763 **References**

764

- 765 Allen, P.A., 2007. The Huqf Supergroup of Oman: Basin development and context for  
766 Neoproterozoic glaciation. *Earth-Science Reviews* 84, 139-185.
- 767 Archer, S.G., Alsop, G.I., Hartley, A.J., Grant, N.T., Hodgkinson, R., 2012. Salt  
768 tectonics, sediments and prospectivity: an introduction, in: Alsop, G.I., Archer, S.G.,  
769 Hartley, A.J., Grant, N.T., Hodgkinson, R. (Eds.), *Salt Tectonics, Sediments and*  
770 *Prospectivity*, pp. 1-6.
- 771 Badhe, K.V., Pandalai, H.S., 2015. Investigations on the Possible Re-equilibration of  
772 Aqueous Fluid Inclusions in Barite: A Study of Barite and Calcite from the Hutti Gold  
773 Deposit, Karnataka, India. *Acta Geol. Sin.-Engl. Ed.* 89, 715-725.
- 774 Balsamo, F., Clemenzi, L., Storti, F., Mozafari, M., Solum, J., Swennen, R., Taberner,  
775 C., Tueckmantel, C., 2016. Anatomy and paleofluid evolution of laterally restricted  
776 extensional fault zones in the Jabal Qusaybah anticline, Salakh arch, Oman.  
777 *Geological Society of America Bulletin* 128, 957-972.

- 778 Banerjee, D.M., Strauss, H., Bhattacharya, S.K., Kumar, V., Mazumdar, A., 1998.  
779 Isotopic composition of carbonates and sulphates, potash mineralisation and basin  
780 architecture of the Nagaur-Gangnagar evaporite basin (northwestern India) and their  
781 implications on the Neoproterozoic exogenic cycle. *Mineralogical Magazine* 62A,  
782 106-107.
- 783 Béchenec, F., Le Métour, J., Platel, J.P., Roger, J., 1993. Geological map of the  
784 Sultanate of Oman. Ministry of Petroleum and Minerals, Sultanate of Oman.
- 785 Bechtel, A., Shieh, Y.N., Pervaz, M., Puttmann, W., 1996. Biodegradation of  
786 hydrocarbons and biogeochemical sulfur cycling in the salt dome environment:  
787 Inferences from sulfur isotope and organic geochemical investigations of the Bahloul  
788 Formation at the Bou Grine Zn/Pb ore deposit, Tunisia. *Geochimica Et*  
789 *Cosmochimica Acta* 60, 2833-2855.
- 790 Bertram, M.A., Cowen, J.P., 1997. Morphological and compositional evidence for  
791 biotic precipitation of marine barite. *Journal of Marine Research* 55, 577-593.
- 792 Blount, C.W., 1977. Barite solubilities and thermodynamic quantities up to 300°C and  
793 1400 bars. *American Mineralogist* 62, 942-957.
- 794 Bons, P.D., 2001. The formation of large quartz veins by rapid ascent of fluids in  
795 mobile hydrofractures. *Tectonophysics* 336, 1-17.
- 796 Bons, P.D., Elburg, M.A., Gomez-Rivas, E., 2012. A review of the formation of  
797 tectonic veins and their microstructures. *Journal of Structural Geology* 43, 33-62.
- 798 Bottrell, S.H., Newton, R.J., 2006. Reconstruction of changes in global sulfur cycling  
799 from marine sulfate isotopes. *Earth-Science Reviews* 75, 59-83.
- 800 Burns, S.J., Haudenschild, U., Matter, A., 1994. The strontium isotopic composition  
801 of carbonates from the late Precambrian (approximate-to-560-540 Ma) Huqf Group of  
802 Oman. *Chemical Geology* 111, 269-282.
- 803 Cai, C.F., Hu, G.Y., He, H., Li, J., Li, J.F., Wu, Y.S., 2005. Geochemical  
804 characteristics and origin of natural gas and thermochemical sulphate reduction in  
805 Ordovician carbonates in the Ordos Basin, China. *Journal of Petroleum Science and*  
806 *Engineering* 48, 209-226.
- 807 Claringbould, J.S., Hyden, B.B., Sarg, J.F., Trudgill, B.D., 2013. Structural evolution  
808 of a salt-cored, domed, reactivated fault complex, Jebel Madar, Oman. *Journal of*  
809 *Structural Geology* 51, 118-131.
- 810 Claypool, G.E., Holser, W.T., Kaplan, I.R., Sakai, H., Zak, I., 1980. The age curves of  
811 sulfur and oxygen isotopes in marine sulfate and their mutual interpretation.  
812 *Chemical Geology* 28, 199-260.
- 813 Dehairs, F., Chesselet, R., Jedwab, J., 1980. Discrete suspended particles of barite  
814 and the barium cycle in the open ocean. *Earth and Planetary Science Letters* 49,  
815 528-550.
- 816 Demeny, A., Kele, S., Siklosy, Z., 2010. Empirical equations for the temperature  
817 dependence of calcite-water oxygen isotope fractionation from 10 to 70 degrees C.  
818 *Rapid Communications in Mass Spectrometry* 24, 3521-3526.
- 819 Dickson, J.A.D., 1966. Carbonate identification and genesis as revealed by staining.  
820 *Journal of Sedimentary Petrology* 36, 491-505.
- 821 Droste, H., van Steenwinkel, M., 2004. Stratal geometries and patterns of platform  
822 carbonates: The Cretaceous of Oman, in: Eberli, G.P., Masaferrro, J.L., Sarg, J.F.R.  
823 (Eds.), *Seismic imaging of carbonate reservoirs and systems*. AAPG Memoir, pp.  
824 185-206.
- 825 Dunn, K., Daniel, E., Shuler, P.J., Chen, H.J., Tang, Y.C., Yen, T.F., 1999.  
826 Mechanisms of surface precipitation and dissolution of barite: A morphology  
827 approach. *Journal of Colloid and Interface Science* 214, 427-437.
- 828 Edgell, H.S., 1991. Proterozoic salt basins of the Persian Gulf area and their role in  
829 hydrocarbon generation. *Precambrian Research* 54, 1-14.
- 830 Ericsson, J.B., McKean, H.C., Hooper, R.J., 1998. Facies and curvature controlled  
831 3D fracture models in a Cretaceous carbonate reservoir, Arabian Gulf, in: Jones, G.,

- 832 Fischer, Q.J., Knipe, R.J. (Eds.), Faulting, fault sealing and fluid flow in hydrocarbon  
833 reservoirs. Geological Society of London, Special Publications, pp. 299-312.
- 834 Evans, D.G., Nunn, J.A., Hanor, J.S., 1991. Mechanisms driving groundwater-flow  
835 near salt domes. *Geophysical Research Letters* 18, 927-930.
- 836 Farzadi, P., 2006. The development of Middle Cretaceous carbonate platforms,  
837 Persian Gulf, Iran: constraints from seismic stratigraphy, well and biostratigraphy.  
838 *Petroleum Geoscience* 12, 59-68.
- 839 Feng, D., Roberts, H.H., 2011. Geochemical characteristics of the barite deposits at  
840 cold seeps from the northern Gulf of Mexico continental slope. *Earth and Planetary  
841 Science Letters* 309, 89-99.
- 842 Fleitmann, D., Burns, S.J., Neff, U., Mangini, A., Matter, A., 2003. Changing moisture  
843 sources over the last 330,000 yrs in northern Oman from fluid inclusion evidence in  
844 speleothems. *Quaternary Research* 60, 223-232.
- 845 Friedman, I., O'Neil, J.R., 1977. Chapter KK. Compilation of stable isotope  
846 fractionation factors of geochemical interest, in: Fleisher, M. (Ed.), *Data of  
847 Geochemistry*. United States Government Printing Office, Washington.
- 848 Gamboa, D., Alves, T.M., 2016. Bi-modal deformation styles in confined mass-  
849 transport deposits: Examples from a salt minibasin in SE Brazil. *Marine Geology* 379,  
850 176-193.
- 851 Glennie, K.W., 2005. *The geology of the Oman Mountains: an outline of their origin.*  
852 Cambrian Printers, Great Britain, Aberystwyth.
- 853 Goldstein, R.H., Reynolds, T.J., 1994. Systematics of fluid inclusions in diagenetic  
854 minerals.
- 855 Gomez-Rivas, E., Bons, P.D., Koehn, D., Urai, J.L., Arndt, M., Virgo, S., Laurich, B.,  
856 Zeeb, C., Stark, L., Blum, P., 2014. THE JABAL AKHDAR DOME IN THE OMAN  
857 MOUNTAINS: EVOLUTION OF A DYNAMIC FRACTURE SYSTEM. *American  
858 Journal of Science* 314, 1104-1139.
- 859 Gradmann, S., Beaumont, C., Ings, S.J., 2012. Coupled fluid flow and sediment  
860 deformation in margin-scale salt-tectonic systems: 1. Development and application of  
861 simple, single-lithology models. *Tectonics* 31.
- 862 Greinert, J., Bollwerk, S.M., Derkachev, A., Bohrmann, G., Suess, E., 2002. Massive  
863 barite deposits and carbonate mineralization in the Derugin Basin, Sea of Okhotsk:  
864 precipitation processes at cold seep sites. *Earth and Planetary Science Letters* 203,  
865 165-180.
- 866 Griffith, E.M., Paytan, A., 2012. Barite in the ocean - occurrence, geochemistry and  
867 palaeoceanographic applications. *Sedimentology* 59, 1817-1835.
- 868 Hallager, W.S., Ulrich, M.R., Kyle, J.R., Price, P.E., Gose, W.A., 1990. Evidence for  
869 episodic basin dewatering in salt-dome cap rocks. *Geology* 18, 716-719.
- 870 Hanor, J.S., 1994. Origin of saline fluids in sedimentary basins, in: Parnell, J. (Ed.),  
871 *Geofluids: Origin, Migration and Evolution of Fluids in Sedimentary Basins.*  
872 Geological Society Special Publications, pp. 151-174.
- 873 Hanor, J.S., 2000. Barite-celestine geochemistry and environments of formation.  
874 *Sulfate Minerals - Crystallography, Geochemistry and Environmental Significance* 40,  
875 193-275.
- 876 Holzbecher, E., Kohfahl, C., Mazurowski, M., Bacik, A., Dobies, M., Schneider, M.,  
877 2010. The Sensitivity of Thermohaline Groundwater Circulation to Flow and  
878 Transport Parameters: A Numerical Study Based on Double-Diffusive Convection  
879 above a Salt Dome. *Transport in Porous Media* 83, 771-791.
- 880 Hudec, M.R., Jackson, M.P.A., 2007. *Terra infirma: Understanding salt tectonics.*  
881 *Earth-Science Reviews* 82, 1-28.
- 882 Immenhauser, A., Dublyansky, Y.V., Verwer, K., Fleitmann, D., Pashenko, S.E.,  
883 2007. Textural, elemental, and isotopic characteristics of Pleistocene phreatic cave  
884 deposits (Jabal Madar, Oman). *Journal of Sedimentary Research* 77, 68-88.

- 885 Jackson, C.A.L., Lewis, M.M., 2016. Structural style and evolution of a salt-influenced  
886 rift basin margin; the impact of variations in salt composition and the role of polyphase  
887 extension. *Basin Research* 28, 81-102.
- 888 Jackson, M.P.A., Vendeville, B.C., 1994. Regional extension as a geologic trigger for  
889 diapirism. *Geological Society of America Bulletin* 106, 57-73.
- 890 John, C.M., Vandeginste, V., Jourdan, A.-L., Kluge, T., Davis, S., Sena, C., Hönig,  
891 M., Beckert, J., 2014. Carbonate reservoir analogues and clumped isotopes: How  
892 combined geometries and geochemistry of outcrops help reservoir management in  
893 the Middle East. *IPTC Conference Paper*, 17256.
- 894 Kusakabe, M., Robinson, B.W., 1977. Oxygen and sulfur isotope equilibrium in BaSO<sub>4</sub>-  
895 HSO<sub>4</sub>-H<sub>2</sub>O system from 110 to 350-degrees-C and applications. *Geochimica Et*  
896 *Cosmochimica Acta* 41, 1033-1040.
- 897 Longinelli, A., Craig, H., 1967. Oxygen-18 variations in sulfate ions in sea water and  
898 saline lakes. *Science (New York, N.Y.)* 156, 56-59.
- 899 Loosveld, R.J.H., Bell, A., Terken, J.J.M., 1996. The tectonic evolution of interior  
900 Oman. *GeoArabia* 1, 28-50.
- 901 Machel, H.G., 2001. Bacterial and thermochemical sulfate reduction in diagenetic  
902 settings - old and new insights. *Sedimentary Geology* 140, 143-175.
- 903 Mann, A., Hanna, S.S., 1990. The tectonic evolution of pre-Permian rocks, Central  
904 and Southeastern Oman Mountains, in: Robertson, A.H.F., Searle, M.P., Ries, A.C.  
905 (Eds.), *The Geology and Tectonics of the Oman Region*. Geological Society Special  
906 Publication, London, pp. 307-325.
- 907 Marchev, P., Downes, H., Thirlwall, M.F., Mortiz, R., 2002. Small-scale variations of  
908 <sup>87</sup>Sr/<sup>86</sup>Sr isotope composition of barite in the Madjarovo low-sulphidation epithermal  
909 system, SE Bulgaria: implications for sources of Sr, fluid fluxes and pathways of the  
910 ore-forming fluids. *Mineralium Deposita* 37, 669-677.
- 911 Mattes, B.W., Morris, S.C., 1990. Carbonate evaporite deposition in the late  
912 Precambrian - early Cambrian Ara Formation of southern Oman, in: Robertson,  
913 A.H.F., Searle, M.P., Ries, A.C. (Eds.), *Geology and Tectonics of the Oman Region*.  
914 Geological Society of London, Special Publications, pp. 617-636.
- 915 Mattos, N.H., Alves, T.M., Omosanya, K.O., 2016. Crestal fault geometries reveal  
916 late halokinesis and collapse of the Samson Dome, Northern Norway: Implications  
917 for petroleum systems in the Barents Sea. *Tectonophysics* 690, 76-96.
- 918 Morrison, S.J., Parry, W.T., 1986. Formation of carbonate-sulfate veins associated  
919 with copper ore-deposits from saline basin brines, Lisbon Valley, Utah - fluid  
920 inclusion and isotopic evidence. *Economic Geology* 81, 1853-1866.
- 921 Mount, V.S., Crawford, R.I.S., Bergman, S.C., 1998. Regional structural style of the  
922 central and southern Oman Mountains: Jebel Akhdar, Saih Hatat, and the Northern  
923 Ghaba Basin. *GeoArabia* 3, 475-490.
- 924 Mozafari, M., Swennen, R., Balsamo, F., Clemenzi, L., Storti, F., El Desouky, H.,  
925 Vanhaecke, F., Tueckmantel, C., Solum, J., Taberner, C., 2015. Paleofluid evolution  
926 in fault-damage zones: evidence from fault-fold interaction events in the Jabal  
927 Qusaybah anticline (Adam Foothills, North Oman). *Journal of Sedimentary Research*  
928 85, 1525-1551.
- 929 Omosanya, K.d.O., Alves, T.M., 2013. Ramps and flats of mass-transport deposits  
930 (MTDs) as markers of seafloor strain on the flanks of rising diapirs (Espírito Santo  
931 Basin, SE Brazil). *Marine Geology* 340, 82-97.
- 932 Paytan, A., Kastner, M., Campbell, D., Thiemens, M.H., 2004. Seawater sulfur  
933 isotope fluctuations in the cretaceous. *Science* 304, 1663-1665.
- 934 Pe-Piper, G., Piper, D.J.W., Zhang, Y.X., Chavez, I., 2015. Diagenetic barite and  
935 sphalerite in middle Mesozoic sandstones, Scotian Basin, as tracers for basin  
936 hydrology. *AAPG Bulletin* 99, 1281-1313.
- 937 Peters, J.M., Filbrandt, J., Grotzinger, J., Newall, M., Shuster, M., Al-Siyabi, H., 2003.  
938 Surface-piercing salt domes in the interior North Oman, and their significance for the  
939 Ara carbonate 'stringer' hydrocarbon play. *GeoArabia* 8, 1-40.



- 940 Quinta, A., Tavani, S., Roca, E., 2012. Fracture pattern analysis as a tool for  
941 constraining the interaction between regional and diapir-related stress fields: Poza de  
942 la Sal Diapir (Basque Pyrenees, Spain), in: Alsop, G.I., Archer, S.G., Hartley, A.J.,  
943 Grant, N.T., Hodgkinson, R. (Eds.), *Salt Tectonics, Sediments and Prospectivity*, pp.  
944 521-532.
- 945 Ramseyer, K., Amthor, J.E., Spötl, C., Terken, J.J.M., Matter, A., Vroon-ten Hove,  
946 M., Borgomano, J.R.F., 2004. Impact of basin evolution, depositional environment,  
947 pore water evolution and diagenesis on reservoir-quality of Lower Paleozoic Haima  
948 Supergroup sandstones, Sultanate of Oman. *GeoArabia* 9, 107-138.
- 949 Ranganathan, V., 1992. Basin dewatering near salt domes and formation of brine  
950 plumes. *Journal of Geophysical Research-Solid Earth* 97, 4667-4683.
- 951 Ranganathan, V., Hanor, J.S., 1989. Perched brine plumes above salt domes and  
952 dewatering of geopressured sediments. *Journal of Hydrology* 110, 63-86.
- 953 Rees, C.E., Jenkins, W.J., Monster, J., 1978. Sulfur isotopic composition of ocean  
954 water sulfate. *Geochimica Et Cosmochimica Acta* 42, 377-381.
- 955 Reuning, L., Schoenherr, J., Heimann, A., Urai, J.L., Littke, R., Kukla, P.A., Rawahi,  
956 Z., 2009. Constraints on the diagenesis, stratigraphy and internal dynamics of the  
957 surface-piercing salt domes in the Ghaba Salt Basin (Oman): A comparison to the  
958 Ara Group in the South Oman Salt Basin. *GeoArabia* 14, 83-120.
- 959 Sarkar, A., Nunn, J.A., Hanor, J.S., 1995. Free thermohaline convection beneath  
960 allochthonous salt sheets - an agent for salt dissolution and fluid-flow in Gulf-Coast  
961 sediments. *Journal of Geophysical Research-Solid Earth* 100, 18085-18092.
- 962 Sassen, R., Cole, G.A., Drozd, R., Roberts, H.H., 1994. Oligocene to Holocene  
963 hydrocarbon migration and salt-dome carbonates, northern Gulf-of-Mexico. *Marine*  
964 *and Petroleum Geology* 11, 55-65.
- 965 Saunders, J.A., Thomas, R.C., 1996. Origin of 'exotic' minerals in Mississippi salt  
966 dome cap rocks: Results of reaction-path modeling. *Applied Geochemistry* 11, 667-  
967 676.
- 968 Schoenherr, J., Reuning, L., Kukla, P.A., Littke, R., Urai, J.L., Siemann, M., Rawahi,  
969 Z., 2009. Halite cementation and carbonate diagenesis of intra-salt reservoirs from  
970 the Late Neoproterozoic to Early Cambrian Ara Group (South Oman Salt Basin).  
971 *Sedimentology* 56, 567-589.
- 972 Schoenherr, J., Schlöder, Z., Urai, J.L., Littke, R., Kukla, P.A., 2010. Deformation  
973 mechanisms of deeply buried and surface-piercing Late Pre-Cambrian to Early  
974 Cambrian Ara Salt from interior Oman. *International Journal of Earth Sciences* 99,  
975 1007-1025.
- 976 Schroder, S., Schreiber, B.C., Amthor, J.E., Matter, A., 2003. A depositional model  
977 for the terminal Neoproterozoic Early Cambrian Ara Group evaporites in south Oman.  
978 *Sedimentology* 50, 879-898.
- 979 Schroder, S., Schreiber, B.C., Amthor, J.E., Matter, A., 2004. Stratigraphy and  
980 environmental conditions of the terminal Neoproterozoic-Cambrian period in Oman:  
981 evidence from sulphur isotopes. *J. Geol. Soc.* 161, 489-499.
- 982 Shikazono, N., 1994. Precipitation mechanisms of barite in sulfate-sulfide deposits in  
983 back-arc basins. *Geochimica Et Cosmochimica Acta* 58, 2203-2213.
- 984 Sibson, R.H., 1992. Fault-valve behavior and the hydrostatic lithostatic fluid pressure  
985 interface. *Earth-Science Reviews* 32, 141-144.
- 986 Smith, A.P., Fischer, M.P., Evans, M.A., 2012. Fracture-controlled palaeohydrology  
987 of a secondary salt weld, La Popa Basin, NE Mexico, in: Alsop, G.I., Archer, S.G.,  
988 Hartley, A.J., Grant, N.T., Hodgkinson, R. (Eds.), *Salt Tectonics, Sediments and*  
989 *Prospectivity*, pp. 107-130.
- 990 Souissi, F., Sasst, R., Dandurand, J.-L., Bouhleb, S., Ben Hamdal, S., 2007. Fluid  
991 inclusion microthermometry and rare earth element distribution in the celestites of the  
992 Jebel Doghra ore deposit (Dome Zone, northern Tunisia): towards a new genetic  
993 model. *Bulletin De La Societe Geologique De France* 178, 459-471.

- 994 Staude, S., Bons, P.D., Markl, G., 2009. Hydrothermal vein formation by extension-  
995 driven dewatering of the middle crust: An example from SW Germany. *Earth and*  
996 *Planetary Science Letters* 286, 387-395.
- 997 Strauss, H., Banerjee, D.M., Kumar, V., 2001. The sulfur isotopic composition of  
998 Neoproterozoic to early Cambrian seawater - evidence from the cyclic Hanseran  
999 evaporites, NW India. *Chemical Geology* 175, 17-28.
- 1000 Terken, J.M.J., Frewin, N.L., Indrelid, S.L., 2001. Petroleum systems of Oman:  
1001 charge timing and risks. *AAPG Bulletin* 85, 1817-1845.
- 1002 Thirlwall, M.F., 1991. Long-term reproducibility of multicollector Sr and Nd isotope  
1003 ratio analysis. *Chemical Geology* 94, 85-104.
- 1004 Tombros, S.F., Seymour, K.S., Williams-Jones, A.E., Zhai, D., Liu, J., 2015. Origin of  
1005 a barite-sulfide ore deposit in the Mykonos intrusion, cyclades: Trace element,  
1006 isotopic, fluid inclusion and raman spectroscopy evidence. *Ore Geology Reviews* 67,  
1007 139-157.
- 1008 Torres, M.E., Bohrmann, G., Dube, T.E., Poole, F.G., 2003. Formation of modern  
1009 and Paleozoic stratiform barite at cold methane seeps on continental margins.  
1010 *Geology* 31, 897-900.
- 1011 Ulrich, M.R., Bodnar, R.J., 1988. Systematics of stretching of fluid inclusions. 2.  
1012 Barite at 1-atm confining pressure. *Economic Geology* 83, 1037-1046.
- 1013 Vandeginste, V., John, C.M., Manning, C., 2013a. Interplay between depositional  
1014 facies, diagenesis and early fractures in the Early Cretaceous Habshan Formation,  
1015 Jebel Madar, Oman. *Marine and Petroleum Geology* 43, 489-503.
- 1016 Vandeginste, V., John, C.M., van de Flierdt, T., Cosgrove, J.W., 2013b. Linking  
1017 process, dimension, texture and geochemistry in dolomite geobodies: a case study  
1018 from Wadi Mistal (northern Oman). *AAPG Bulletin* 97, 1181-1207.
- 1019 Vandeginste, V., Swennen, R., Gleeson, S.A., Ellam, R.M., Osadetz, K., Roure, F.,  
1020 2006. Development of secondary porosity in the Fairholme carbonate complex  
1021 (southwest Alberta, Canada). *Journal of Geochemical Exploration* 89, 394-397.
- 1022 Vandeginste, V., Swennen, R., Gleeson, S.A., Ellam, R.M., Osadetz, K., Roure, F.,  
1023 2009. Thermochemical sulphate reduction in the Upper Devonian Cairn Formation of  
1024 the Fairholme carbonate complex (South-West Alberta, Canadian Rockies): evidence  
1025 from fluid inclusions and isotopic data. *Sedimentology* 56, 439-460.
- 1026 Vendeville, B.C., 2005. Salt tectonics driven by sediment progradation: Part I -  
1027 Mechanics and kinematics. *AAPG Bulletin* 89, 1071-1079.
- 1028 Wagner, T., Boyce, A.J., Erzinger, J., 2010. FLUID-ROCK INTERACTION DURING  
1029 FORMATION OF METAMORPHIC QUARTZ VEINS: A REE AND STABLE  
1030 ISOTOPE STUDY FROM THE RHENISH MASSIF, GERMANY. *American Journal of*  
1031 *Science* 310, 645-682.
- 1032 Wagner, T., Kirnbauer, T., Boyce, A.J., Fallick, A.E., 2005. Barite-pyrite  
1033 mineralization of the Wiesbaden thermal spring system, Germany: a 500-kyr record  
1034 of geochemical evolution. *Geofluids* 5, 124-139.
- 1035 Wang, T., Yang, C., Ma, H., Daemen, J.J.K., Wu, H., 2015. Safety evaluation of gas  
1036 storage caverns located close to a tectonic fault. *Journal of Natural Gas Science and*  
1037 *Engineering* 23, 281-293.
- 1038 Warren, J.K., 2000. Evaporites, brines and base metals: low-temperature ore  
1039 emplacement controlled by evaporite diagenesis. *Australian Journal of Earth*  
1040 *Sciences* 47, 179-208.
- 1041 Williams, M.D., Ranganathan, V., 1994. Ephemeral thermal and solute plumes  
1042 formed by upwelling groundwaters near salt domes. *Journal of Geophysical*  
1043 *Research-Solid Earth* 99, 15667-15681.
- 1044 Wilson, A., Ruppel, C., 2007. Salt tectonics and shallow subseafloor fluid convection:  
1045 models of coupled fluid-heat-salt transport. *Geofluids* 7, 377-386.
- 1046 Yang, C., Wang, T., Li, Y., Yang, H., Li, J., Qu, D.a., Xu, B., Yang, Y., Daemen,  
1047 J.J.K., 2015. Feasibility analysis of using abandoned salt caverns for large-scale  
1048 underground energy storage in China. *Applied Energy* 137, 467-481.

1049 Yin, H., Groshong, R.H., Jr., 2007. A three-dimensional kinematic model for the  
1050 deformation above an active diapir. *Aapg Bulletin* 91, 343-363.  
1051 Yin, H., Zhang, J., Meng, L., Liu, Y., Xu, S., 2009. Discrete element modeling of the  
1052 faulting in the sedimentary cover above an active salt diapir. *Journal of Structural*  
1053 *Geology* 31, 989-995.  
1054

1055

1056 **Figure captions**

1057

1058 Figure 1. (A) Geological map of northern Oman, simplified after Béchenec et al.  
1059 (1993). (B) Geological map of Jebel Madar, modified after Claringbould et al. (2013).

1060

1061 Figure 2. Overview of stratigraphic units outcropping in Jebel Madar.

1062

1063 Figure 3. Field photographs of barite occurrences. Lens cap (diameter of 58 mm) as  
1064 scale. (A) Lekhwair Formation limestone host rock is cross-cut by vein that contains  
1065 barite (Bar) at the sides and lighter coloured calcite (Cc) in the center. (B) Barite  
1066 tabular crystals (white arrow indicates one) are dispersed within host rock, forming  
1067 fan-shape or radiating patterns (black arrow). (C) Barite, forming layers with some  
1068 radiating patterns. Note the high porosity. (D) Rosettes of cross-cutting tabular barite  
1069 crystals (black arrow).

1070

1071 Figure 4. Microphotographs taken under polarized light (A, C, E) and CL (B, D, F),  
1072 with A & B, C & D and E & F being pairs of images that show the exact same region.  
1073 Scale bar is 500  $\mu\text{m}$ . (A & B) Non-luminescent barite laths and dark orange, dull  
1074 luminescent calcite with some lighter orange luminescent calcite zones. (C & D)  
1075 Coarse fault zone calcite with darker and lighter orange, dull luminescent zonations.  
1076 (E & F) Macro-columnar calcite, which is mainly non-luminescent, with a few thin,  
1077 orange, dull luminescent zonations.

1078

1079 Figure 5. Field photographs of calcite cements. Lens cap (5.8 cm) as scale. (A)  
1080 Relatively thin calcite veins within host rock. (B) Calcite cement (C) in between  
1081 tabular barite (B). (C) Striated fault plane with coarse calcite cementation. Person  
1082 (1.7 m) as scale. (D) Macro-columnar calcite with transparent and reddish coloured  
1083 zones. Marker (14 cm) as scale. (E) Macro-columnar calcite in radiating pattern. Note  
1084 that this calcite cement also occurs along a fault. (F) Calcite rosettes present in the  
1085 same fault zone as the macro-columnar calcite shown in panel C.

1086

1087 Figure 6. Field photographs of cross-cutting of calcite cement phases. Lens cap (5.8  
1088 cm) as scale. (A) Calcite (C) associated with barite (B) cross-cut by reddish brown silt  
1089 layer. (B) Cross-cutting calcite phases and reddish brown silt with speleothems of  
1090 macro-columnar calcite. (C-E) Fault zones with several white calcite, transparent,  
1091 and reddish, macro-columnar calcite vein generations.

1092

1093 Figure 7. Satellite image of Jebel Madar with indication of the occurrence of different  
1094 phases. Most squares on the map represent a set of samples at that locality. Empty  
1095 quarters of the square indicate that the specific corresponding phases were not  
1096 sampled and thus, generally absent. This mapping mainly aimed at reconstructing  
1097 the distribution of barite and major calcite occurrences; hence, the distribution of  
1098 small calcite veins is underrepresented on this figure.

1099

1100 Figure 8. Rose diagrams of structures that contain thin calcite veins, barite-  
1101 associated calcite, fault zone calcite and macro-columnar calcite. Bin size is  $15^\circ$  and  
1102 the circles indicate the number of data points (e.g. barite-associated calcite has  
1103 seven data points which fall in the N30-45 bin).

1104

1105 Figure 9. Crossplot of sulphur isotope versus oxygen isotope signature for barite.  
1106 Each data point represents a measurement from a powder sample drilled from an

1107 individual hand sample (33 data points from 33 different hand samples,  
1108 Supplementary File Table 1). Apart from two outliers, the data form a cluster. The  
1109 rough linear correlation between the two proxies is not significant ( $R^2 = 0.44$ ; two  
1110 outliers excluded). The  $\delta^{18}\text{O}$  is high compared to marine barite and also  $\delta^{34}\text{S}$  is  
1111 relatively high, but similar to that of Late Neoproterozoic to Early Cambrian anhydrite.

1112

1113 Figure 10. Crossplot of stable carbon and oxygen isotopic composition of limestone  
1114 and defined calcite types. Each data point represents a different hand sample, but in  
1115 several occasions multiple hand samples were taken from zones in the same large  
1116 calcite fault zone, fracture or cavern. The distribution shows a clear trend towards  
1117 lower values for both  $\delta^{13}\text{C}$  and  $\delta^{18}\text{O}$  from barite-associated calcite and thin calcite  
1118 veins to fault zone calcite to macro-columnar calcite.

1119

1120 Figure 11. Crossplot of stable oxygen and strontium isotopic composition of  
1121 limestone and defined calcite types. The distribution shows a decrease in average  
1122 strontium isotopic ratio from barite-associated calcite and thin calcite veins to fault  
1123 zone calcite and to macro-columnar calcite. The strontium isotopic composition of the  
1124 Ara Group carbonate in Oman is based on Burns et al. (1994).

1125

1126 Figure 12. Major and minor element contents in defined calcite types. (A) Crossplot  
1127 of Mg versus Sr content, showing a weak positive correlation. (B) Box and whisker  
1128 plot of Mn content, showing a decreasing average value from barite-associated  
1129 calcite to thin calcite veins to fault zone calcite to macro-columnar calcite, similar to  
1130 the trend observed in the stable isotope signature. Note though that the data range  
1131 for the different calcite types overlap.

1132

1133 Figure 13. Photomicrographs of fluid inclusions. (A) Primary single-phase fluid  
1134 inclusions in cluster in barite, and also secondary fluid inclusion trails are present. (B)  
1135 Primary single-phase and two-phase fluid inclusions in cluster barite, and also thin  
1136 trails of very small secondary fluid inclusions. (C) Single-phase fluid inclusions  
1137 interpreted as primary in origin, in barite-associated calcite. (D) Primary isolated  
1138 single-phase fluid inclusions in macro-columnar calcite.

1139

1140 Figure 14. (A) Plot of homogenization temperature versus salinity from fluid inclusion  
1141 measurements in barite. (B) Crossplot of stable oxygen isotope composition of calcite  
1142 versus salinity of fluid inclusions (both primary and secondary) measured in the  
1143 respective calcite sample.

1144

1145 Figure 15. Paragenetic sequence of diagenetic events.

1146

1147 Figure 16. Interpreted structural and paleohydrological evolution (in four time steps)  
1148 presented for a transect through the southwestern part of Jebel Madar. The exact  
1149 location and extent of the Ara salt diapir is uncertain at this location since seismic  
1150 sections are only available from the area surrounding Jebel Madar (Claringbould et  
1151 al., 2013). An early Paleocene time step is not presented here given the maximum  
1152 stress direction was NW-SE at that time which is almost parallel to the orientation of  
1153 the presented transect. The NNE-SSW to NE-SW faults displayed on the transect  
1154 were not active in early Paleocene time and no fluid flow is expected along those  
1155 faults at that time. However, the E-W faults developed as dextral strike-slip faults in  
1156 early Paleocene.

1157

1158 Figure 17. Mixing model indicating geochemical signatures. (A) Mixing model of  
1159 saline (17 wt% NaCl eq) end member fluid at 100°C,  $\delta^{18}\text{O}_{\text{fluid}}$  of +10.9‰ VSMOW and

1160  $^{87}\text{Sr}/^{86}\text{Sr}$  of 0.71023 and meteoric (0 wt% NaCl eq) end member fluid at 35°C,  $\delta^{18}\text{O}_{\text{fluid}}$   
 1161 of -10.4‰ VSMOW and  $^{87}\text{Sr}/^{86}\text{Sr}$  of 0.70884. Note the slightly irregular temperature  
 1162 scale (compared to the meteoric fluid fraction scale) due to the different heat capacity  
 1163 of saline versus meteoric fluid. (B) Mixing model of the same two fluid end members  
 1164 as presented in A showing reconstructed  $\delta^{18}\text{O}_{\text{calcite}}$  and  $\delta^{13}\text{C}_{\text{calcite}}$  (considering 10  
 1165 times higher carbon content in the saline end member compared to the meteoric end  
 1166 member).

1167

### 1168 **Appendix 1.**

1169 The mixing calculations are based on a linear mixing model of two end member  
 1170 components for the determination of salinity,  $^{87}\text{Sr}/^{86}\text{Sr}$  and  $\delta^{18}\text{O}_{\text{fluid}}$ , through the  
 1171 following equation:

$$1172 \quad V_{\text{mix}} = F_1 V_1 + (1 - F_1) V_2$$

1173 where  $V_{\text{mix}}$  is the calculated signature of the mixture,  $F_1$  is the meteoric fluid fraction,  
 1174  $V_1$  is the signature of the meteoric fluid end member and  $V_2$  is the signature of the  
 1175 saline end member fluid.

1176 For the determination of the temperature of the mixed fluid, we need to take account  
 1177 of the different heat capacities of the meteoric end member fluid and the saline end  
 1178 member fluid, through the following equation:

$$1179 \quad T_{\text{mix}} = \frac{F_1}{F_1 + \frac{C_{v2}(1-F_1)}{C_{v1}}} T_1 + \frac{\frac{C_{v2}(1-F_1)}{C_{v1}}}{F_1 + \frac{C_{v2}(1-F_1)}{C_{v1}}} T_2$$

1180 where  $T_{\text{mix}}$  is the calculated temperature of the mixture,  $F_1$  is the meteoric fluid  
 1181 fraction,  $T_1$  is the temperature of the meteoric fluid end member,  $T_2$  is the  
 1182 temperature of the saline end member fluid,  $C_{v1}$  is the heat capacity of the meteoric  
 1183 end member fluid and  $C_{v2}$  is the heat capacity of the saline end member fluid.

1184 Similarly, the stable carbon isotopic composition of the mixture can be calculated by  
 1185 taking account of the different carbon content in the end member fluid:

$$\delta^{13}C_{\text{mix}} = \frac{F_1}{F_1 + \frac{c_2}{c_1}(1-F_1)} \delta^{13}C_1 + \frac{\frac{c_2}{c_1}(1-F_1)}{F_1 + \frac{c_2}{c_1}(1-F_1)} \delta^{13}C_2$$

1186

1187 where  $\delta^{13}C_{\text{mix}}$  is the calculated stable carbon isotope composition of the mixture,  $F_1$  is  
 1188 the meteoric fluid fraction,  $\delta^{13}C_1$  is the stable carbon isotope composition of the  
 1189 meteoric fluid end member,  $\delta^{13}C_2$  is the stable carbon isotope composition of the  
 1190 saline end member fluid,  $c_1$  is the carbon content of the meteoric end member fluid  
 1191 and  $c_2$  is the carbon content of the saline end member fluid.

1192

### 1193 **Supplementary File Table 1**

1194 Table 1. Carbon, oxygen and strontium isotope data of host rock, thin calcite veins,  
 1195 barite-associated calcite, fault zone calcite and macro-columnar calcite. Details of  
 1196 latitude and longitude of sampling are also presented.

1197

### 1198 **Supplementary File Table 2**

1199 Table 2. Geochemical elemental data of host rock, thin calcite veins, barite-  
 1200 associated calcite, fault zone calcite, intermediate calcite and macro-columnar  
 1201 calcite. Details of latitude and longitude of sampling are presented as well.

1202

### 1203 **Supplementary File Table 3**

1204 Table 3. Fluid inclusion data of barite-associated calcite, fault zone calcite, and  
 1205 macro-columnar calcite. T<sub>fm</sub>: temperature of observed first melting, T<sub>m ice</sub>:  
 1206 temperature of final melting of ice, T<sub>h</sub>: homogenization temperature.

1207

### 1208 **Supplementary File Figure 18.**



1209 Figure 18. Histograms of stable carbon and oxygen isotope data measured in the  
1210 different calcite types, and the fluid inclusion final melting temperature of ice data in  
1211 the different diagenetic types.

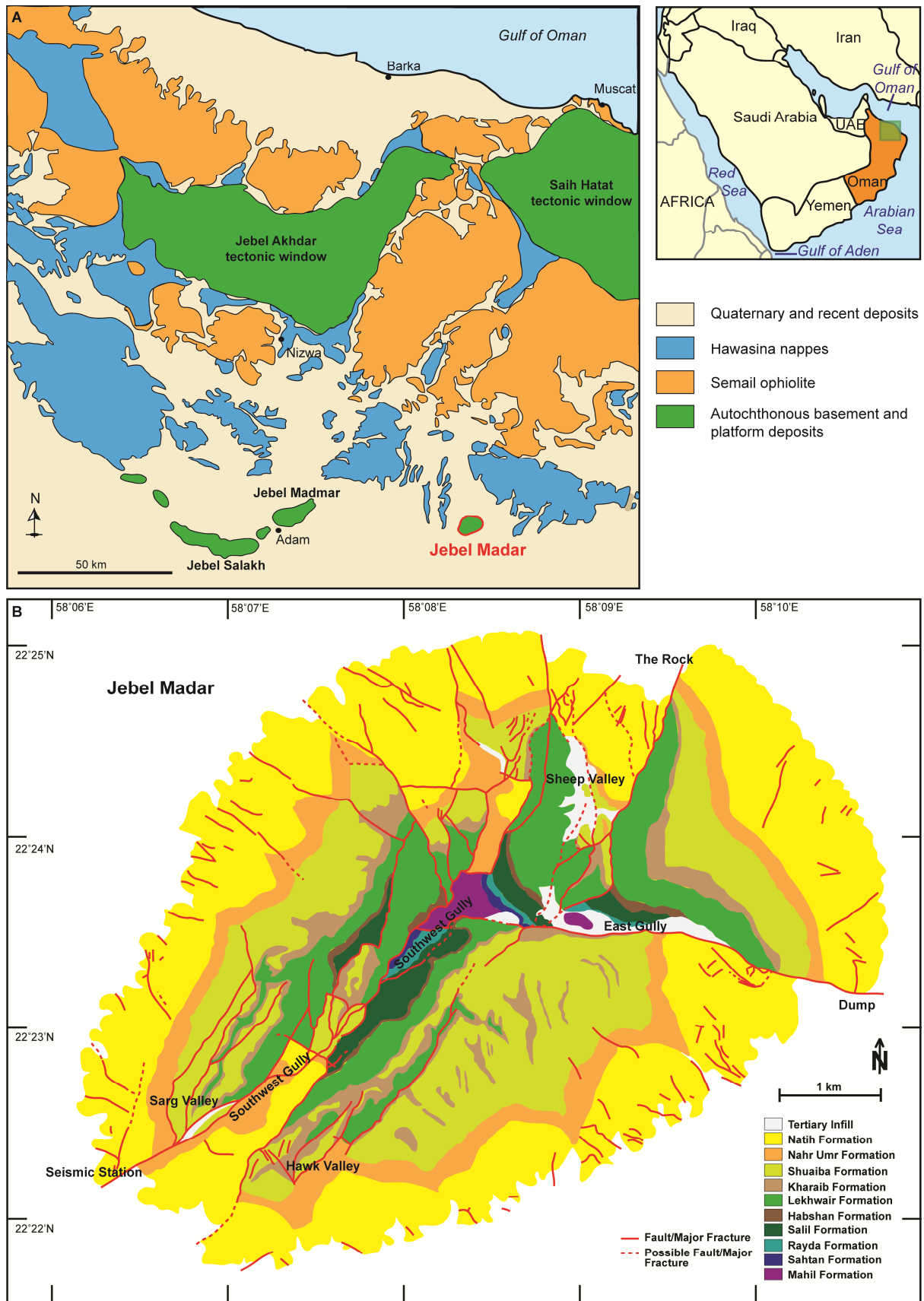
1212



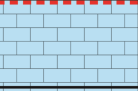
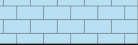
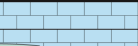


1213

1214








1215

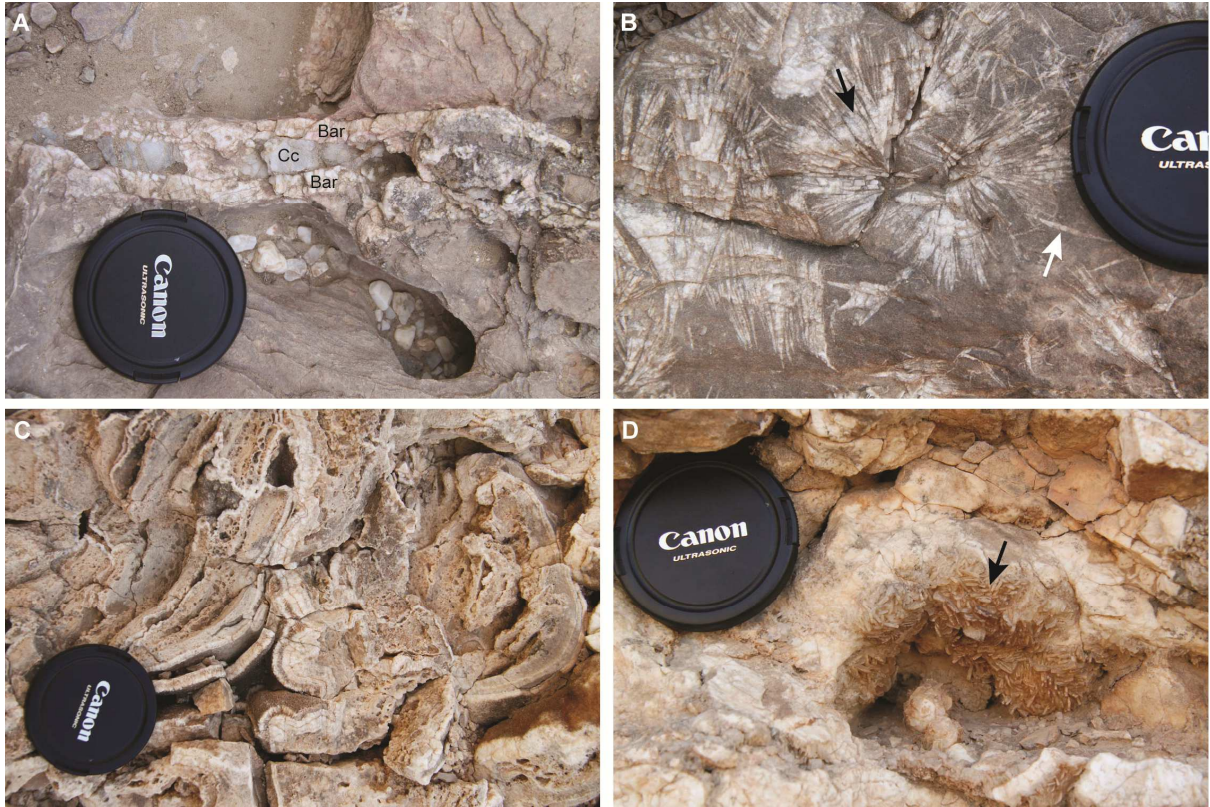
ACCEPTED MANUSCRIPT

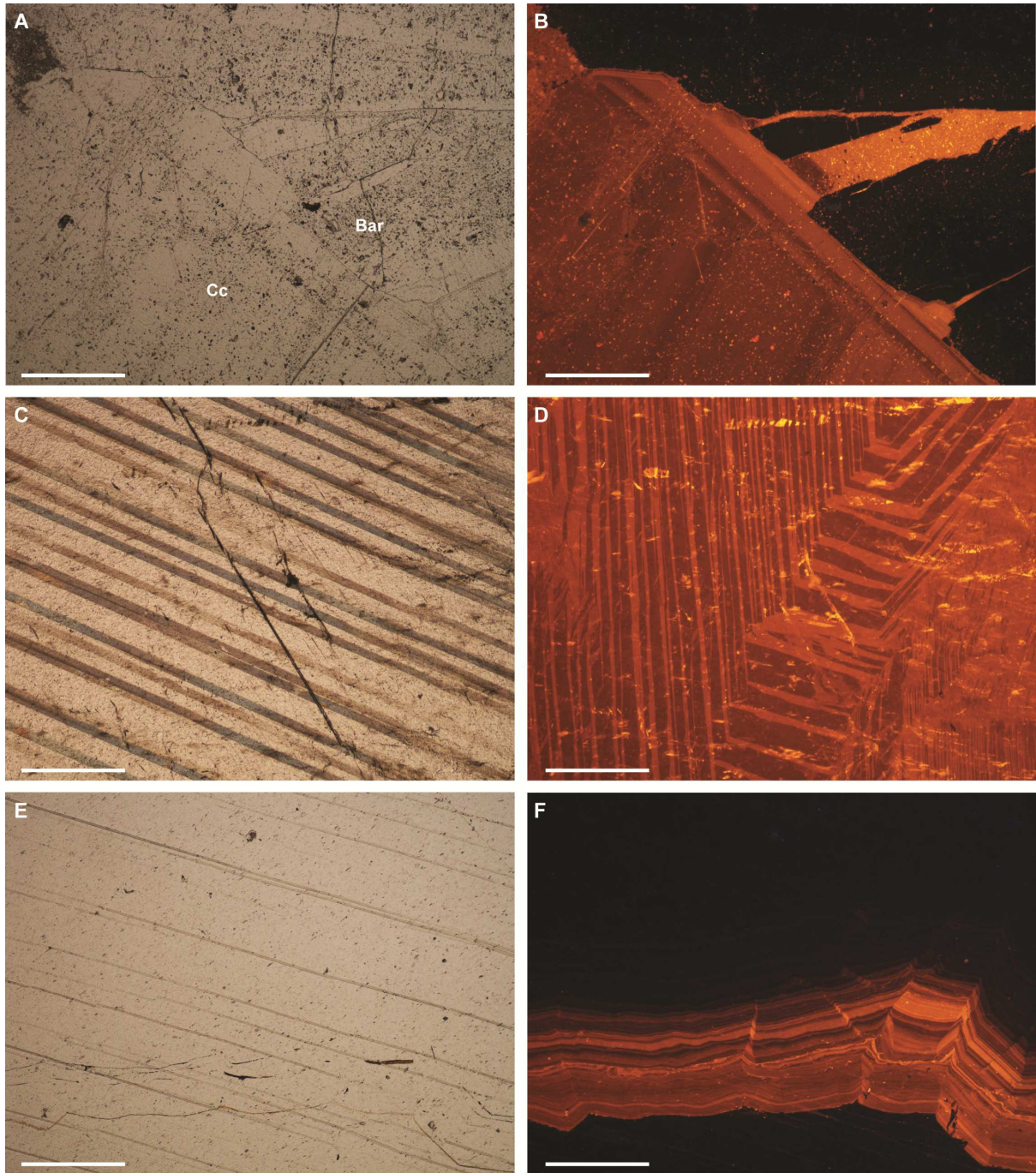


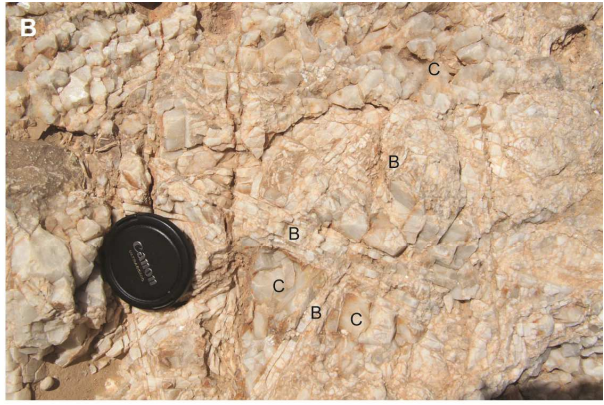
Age (Ma)	Period/Epoch	Group	Lithology	Formation	Thickness (m)					
89	Cretaceous	Wasia		Natih	175					
94						Turonian				
100		Cenomanian								
112		Albian		Nahr Umr	200					
125		Kahmah		Shuaiba	75					
130						Aptian				
134						Barremian				
140						Hauterivian				
146	Valanginian									
146	Jurassic	Sahtan	 	Dhruma Mafraq	150					
200						Triassic	Akhdar	 	Mahil Saiq	200
251										

	Shallow water limestone		Dolomite		Shale
	Deep water limestone		Marl		Sandstone
	Unconformity				

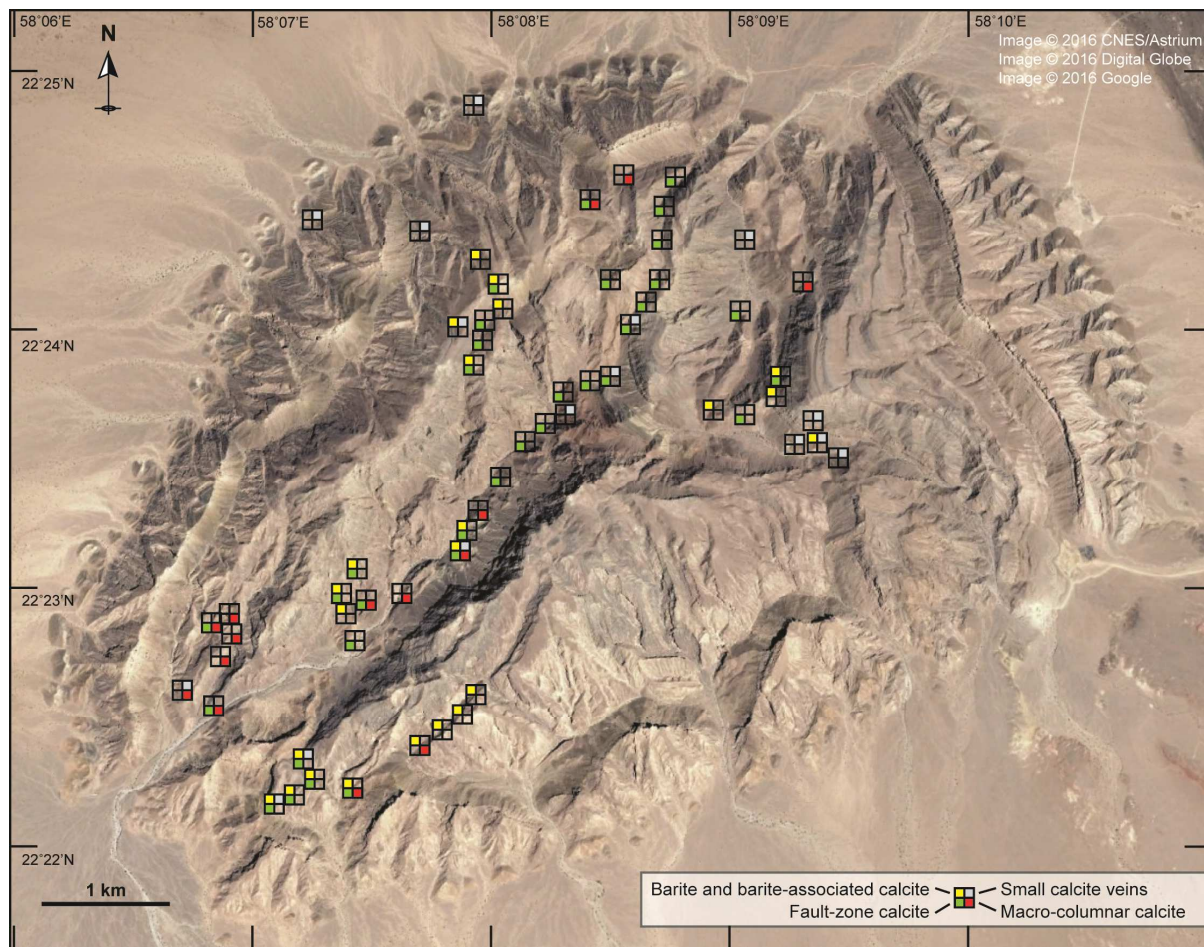




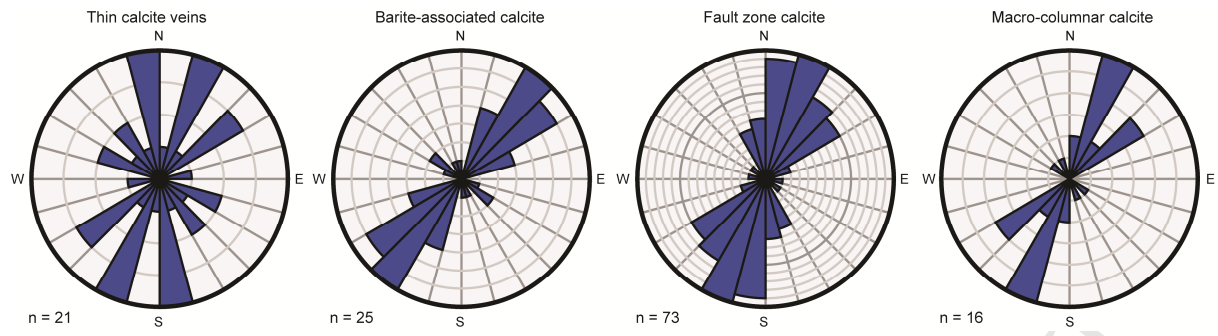


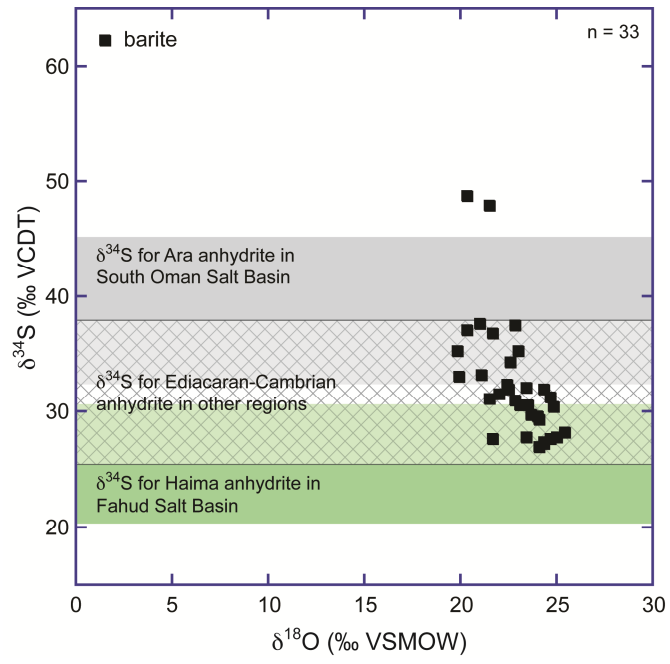


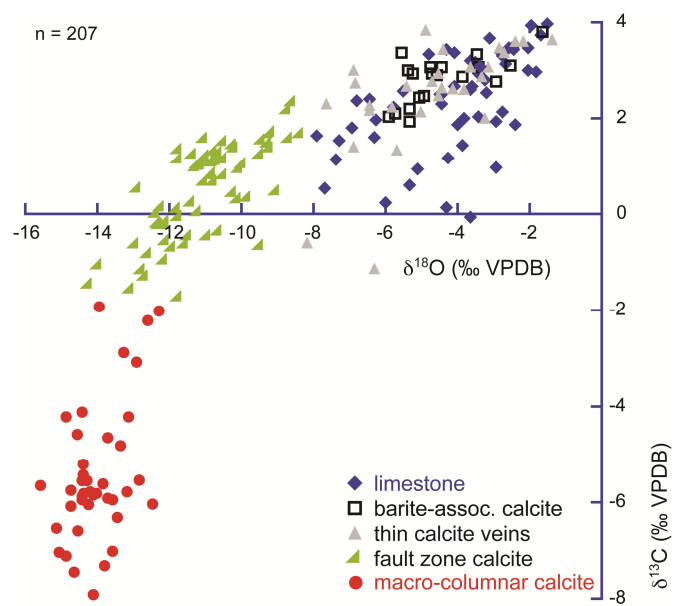
ACCEPTED

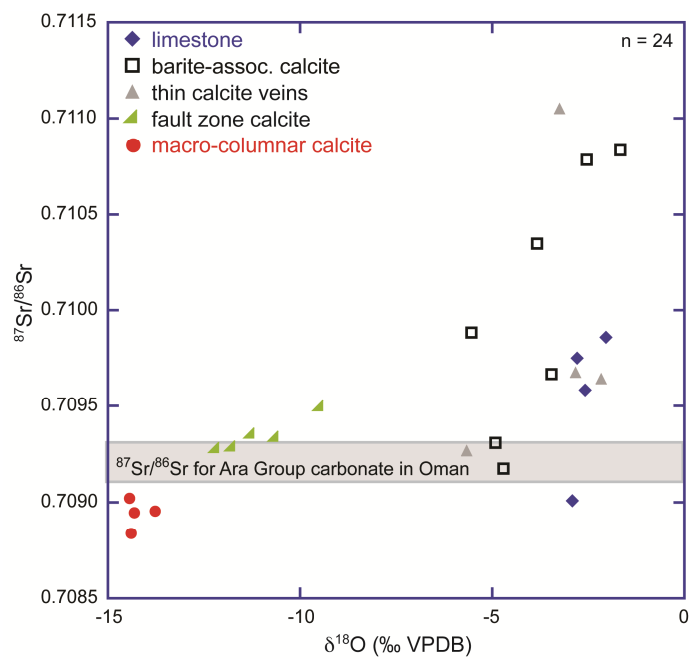


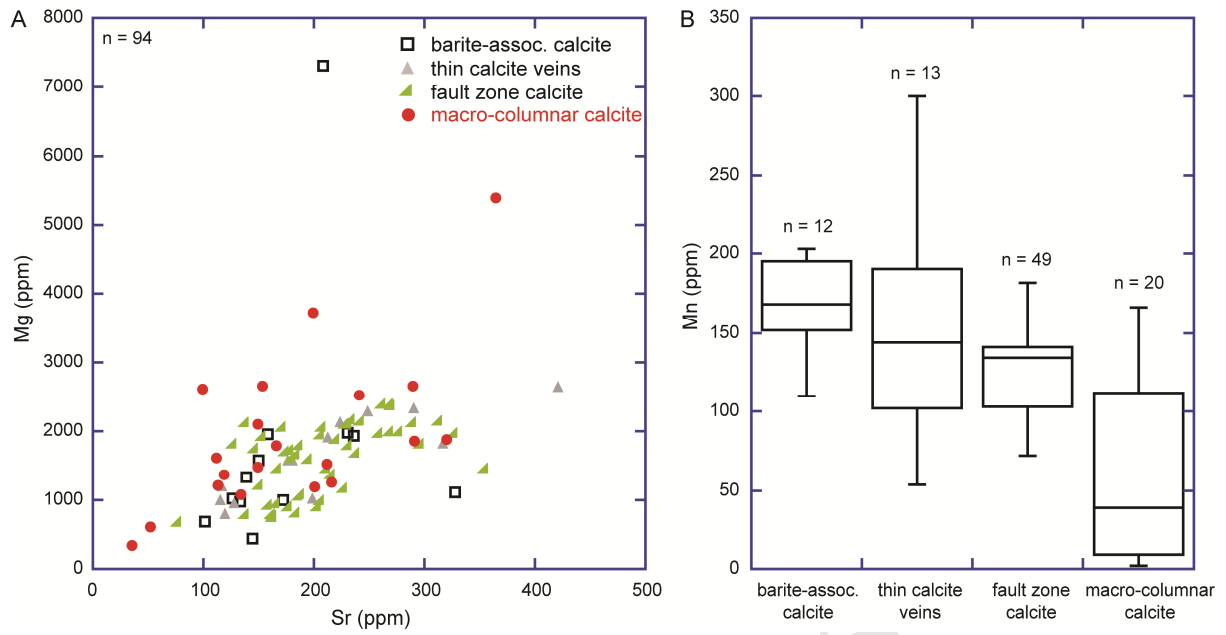


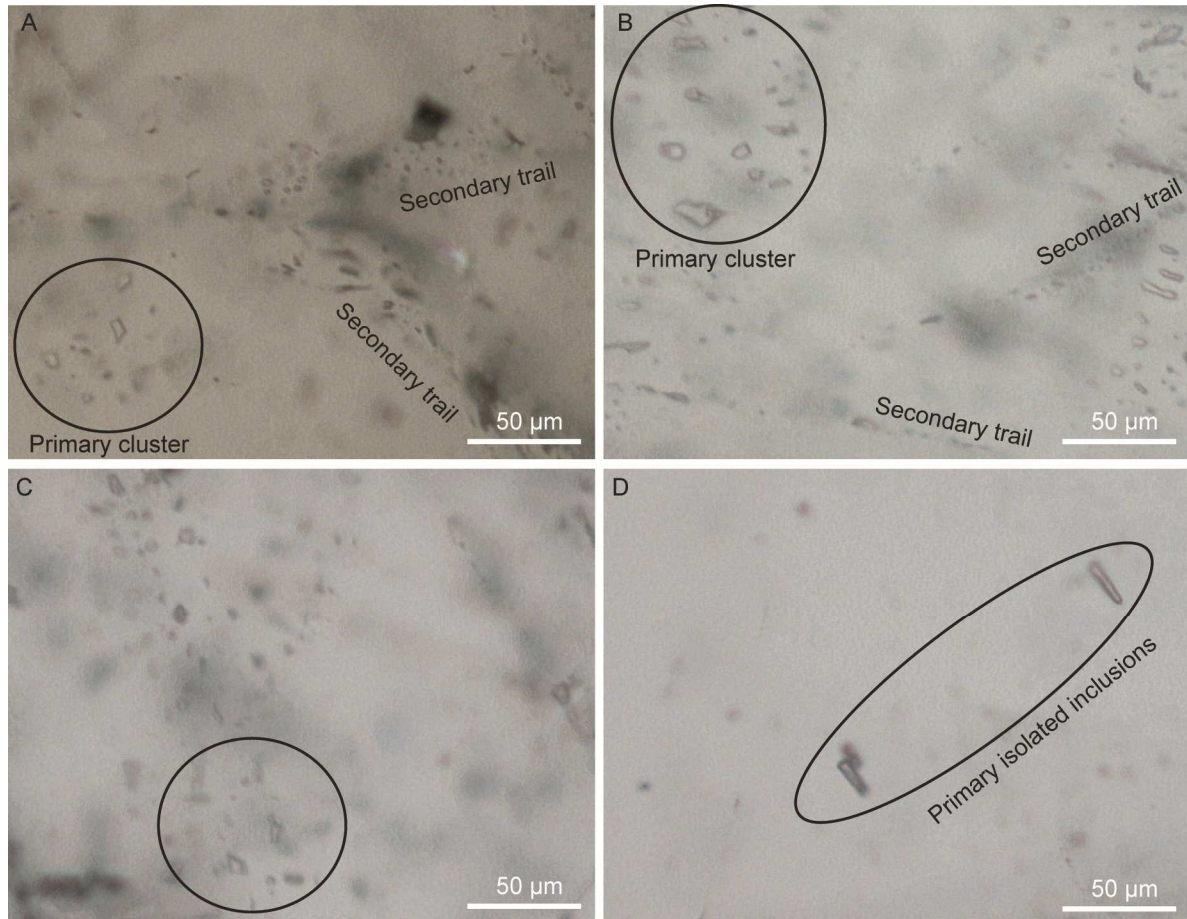




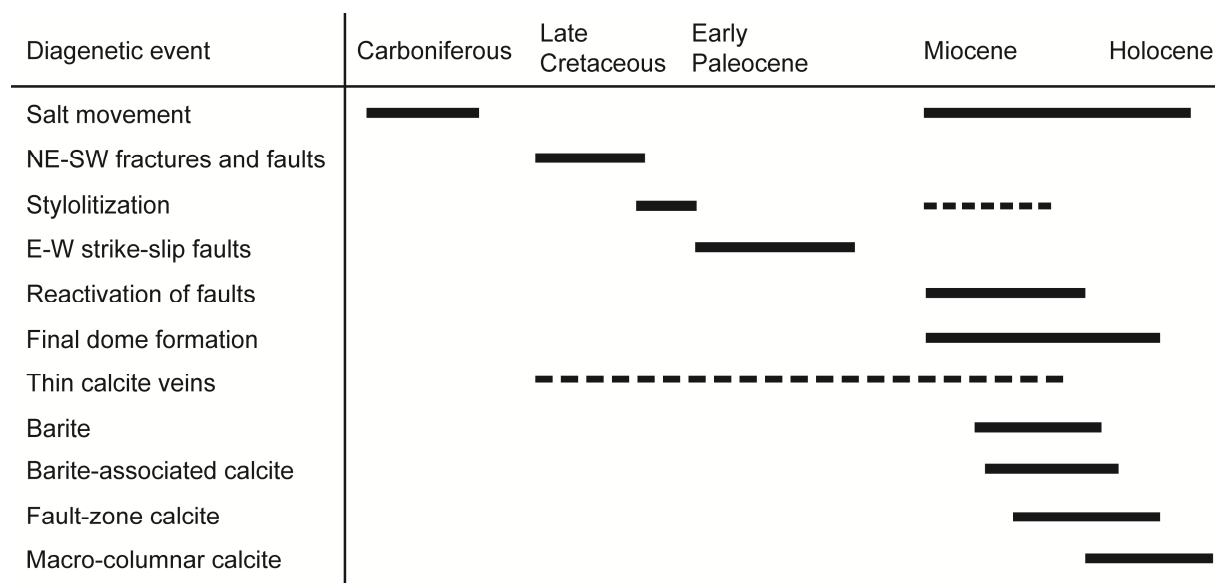






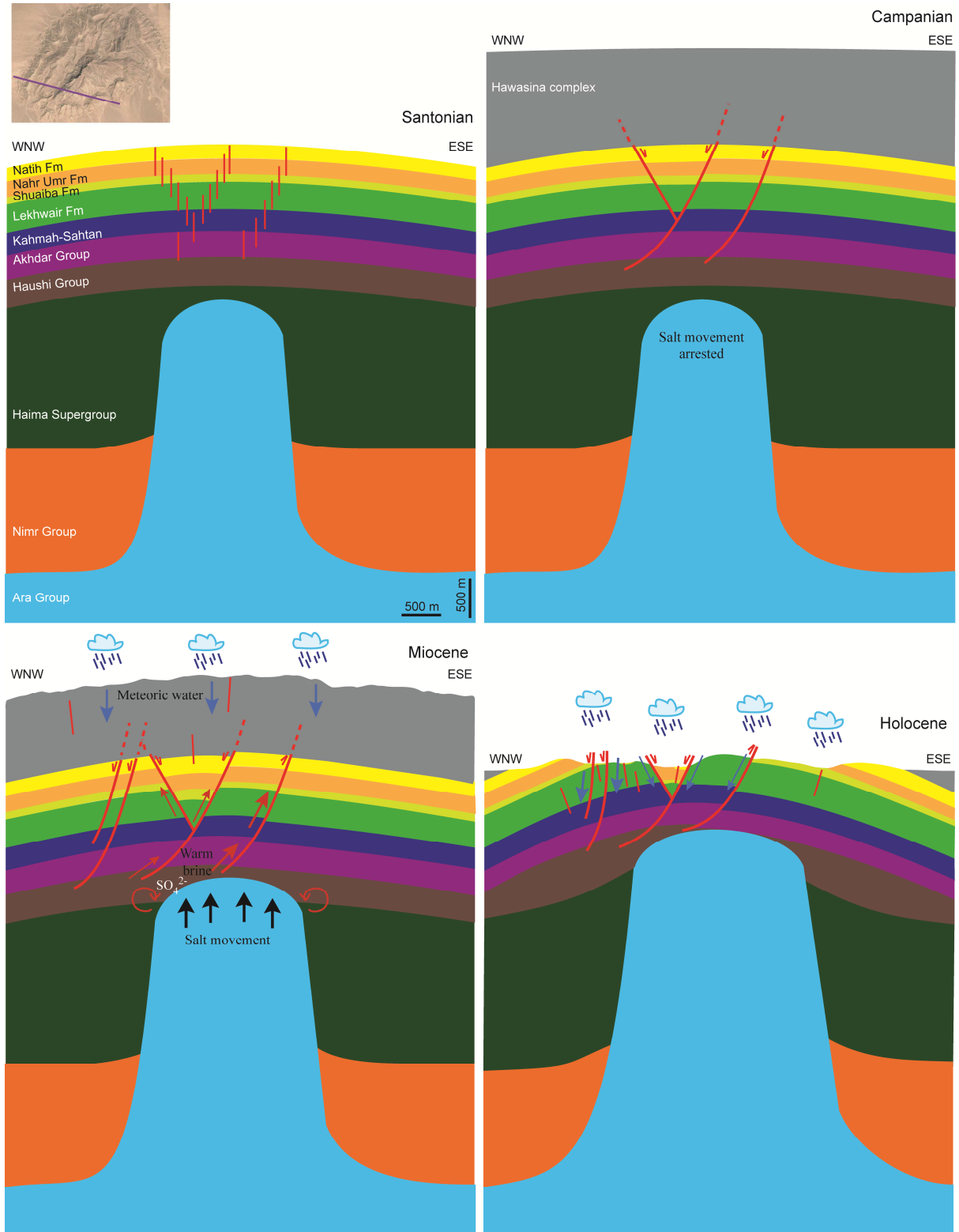


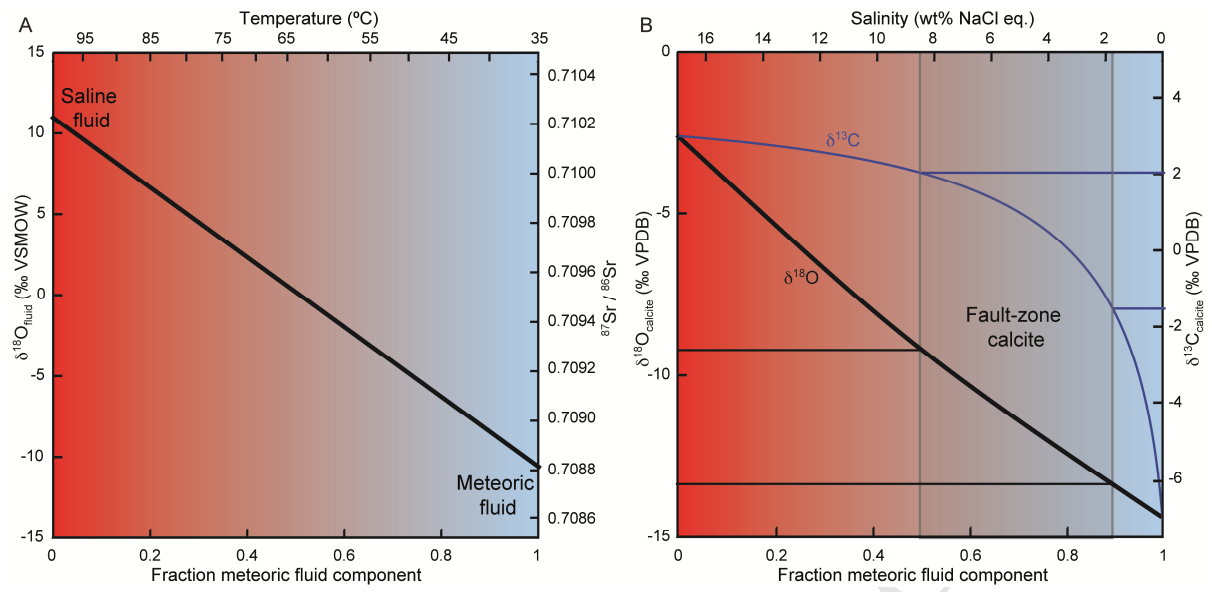




ACCEPTED MANUSCRIPT







**Highlights*****Diagenesis in salt dome roof strata: barite - calcite assemblage in Jebel Madar, Oman***

- The spatial distribution of diagenetic phases in a salt dome in Oman is presented.
- Clear link between structural evolution and fluid flow in salt dome roof strata.
- Barite sulfate source comes from Ara Group evaporite and Haima Supergroup layers.
- Diagenetic products occur mainly along NE-SW to ENE-WSW faults and fractures.
- Warm saline fluids mix progressively with meteoric fluids during Miocene to Pleistocene.